

1 Contribution of expanded marine sulfur chemistry to the seasonal variability 2 of DMS oxidation products and size-resolved sulfate aerosol

3 Linia Tashmim¹, William C. Porter¹, Qianjie Chen², Becky Alexander³, Charles H. Fite⁴,
4 Christopher D. Holmes⁴, Jeffrey R. Pierce⁵, Betty Croft⁶, and Sakiko Ishino⁷

5 ¹Department of Environmental Sciences, University of California, Riverside, CA, USA

6 ²Department of Civil and Environmental Engineering, The Hong Kong Polytechnic University,
7 Hong Kong, China

8 ³Department of Atmospheric Sciences, University of Washington, Seattle, WA, USA

9 ⁴Department of Earth, Ocean and Atmospheric Science, Florida State University, Tallahassee,
10 FL, USA

11 ⁵Department of Atmospheric Science, Colorado State University, Fort Collins, CO, USA

12 ⁶Department of Physics and Atmospheric Science, Dalhousie University, Halifax, Nova Scotia,
13 Canada

14 ⁷Institute of Nature and Environmental Technology, Kanazawa University, Japan

15 Correspondence: Linia Tashmim (ltash001@ucr.edu) and William C. Porter
16 (william.porter@ucr.edu)

17 **Abstract.** Marine emissions of dimethyl sulfide (DMS) and the subsequent formation of its
18 oxidation products methane sulfonic acid (MSA) and sulfuric acid (H₂SO₄) are well-known natural
19 precursors of atmospheric aerosols, contributing to particle mass and cloud formation over ocean
20 and coastal regions. Despite a long-recognized and well-studied role in the marine troposphere,
21 DMS oxidation chemistry remains a work in progress within many current air quality and climate
22 models, with recent advances exploring heterogeneous chemistry and uncovering previously
23 unknown intermediate species. With the identification of additional DMS oxidation pathways and
24 intermediate species influencing its eventual fate, it is important to understand the impact of these
25 pathways on the overall sulfate aerosol budget and aerosol size distribution. In this work, we
26 update and evaluate the DMS oxidation mechanism of the chemical transport model GEOS-Chem
27 by implementing expanded DMS oxidation pathways into the model. These updates include gas-
28 and aqueous-phase reactions, the formation of the intermediates dimethyl sulfoxide (DMSO) and
29 methane sulphinic acid (MSIA), as well as cloud loss and aerosol uptake of the recently quantified
30 intermediate hydroperoxymethyl thioformate (HPMTF). We find that this updated mechanism
31 collectively decreases the global mean surface-layer gas-phase sulfur dioxide (SO₂) mixing ratio
32 by 40% and enhances sulfate aerosol (SO₄²⁻) mixing ratio by 17%. We further perform sensitivity
33 analyses exploring the contribution of cloud loss and aerosol uptake of HPMTF to the overall
34 sulfur budget. Comparing modeled concentrations to available observations we find improved
35 biases relative to previous studies. To quantify impacts of these chemistry updates on global
36 particle size distributions and mass concentration we use the TOMAS aerosol microphysics
37 module coupled to GEOS-Chem, finding changes in particle formation and growth affect the size
38 distribution of aerosol. With this new DMS-oxidation scheme the global annual mean surface layer
39 number concentration of particles with diameters smaller than 80 nm decreases by 16.8%, with
40 cloud loss processes related to HPMTF mostly responsible for this reduction. However, global
41 annual mean number of particles larger than 80 nm increases by 3.8% suggesting that the new
42 scheme promotes seasonal particle growth to these sizes capable of acting as cloud condensation
43 nuclei (CCN).

44 1 Introduction

45 Dimethyl sulfide (DMS: CH_3SCH_3) is the most abundant biological source of sulfate aerosol and
46 has a significant influence on Earth's radiation budget and climate due to its contribution to
47 atmospheric marine particle (Charlson et al., 1987; Fung et al., 2022). In the atmosphere, DMS
48 reacts with hydroxyl radical (OH), nitrate radical (NO_3), ozone (O_3) and various halogen species
49 (e.g., chlorine (Cl) and bromine oxide (BrO)), primarily forming sulfur dioxide (SO_2) and methyl
50 sulfonic acid (MSA: $\text{CH}_3\text{SO}_3\text{H}$) (Chen et al., 2018; Faloon, 2009; Hoffmann et al., 2016). These
51 oxidation products are considered key influences on the formation and evolution of natural
52 aerosols and clouds along with their associated climate impacts, especially in the marine boundary
53 layer (MBL) (Carslaw et al., 2013; Sipilä et al., 2010; Schobesberger et al., 2013; Thomas et al.,
54 2010; von Glasow and Crutzen, 2004). SO_2 and MSA formed by DMS oxidation can be deposited
55 on Earth surface or further oxidize affecting the size distribution of aerosol and cloud microphysics
56 (Leaitch et al., 2013; Wollesen de Jonge et al., 2021). SO_2 can either oxidize in the gas-phase by
57 reaction with the OH radical forming H_2SO_4 , which can participate in nucleation and early growth
58 of particles in the atmosphere, or it can be taken up by cloud droplets and undergo aqueous phase
59 oxidation by reaction with H_2O_2 , O_3 and O_2 catalyzed by transition metals (Mn, Fe) forming SO_4^{2-}
60 and generally only contributing to the growth of aerosol particles (Hoyle et al., 2016; Kulmala,
61 2003; Alexander et al., 2009). The hypohalous acids (HOBr, HOCl, HOI) also plays significant
62 role in aqueous-phase sulfate production in the marine boundary layer (MBL) (Chen et al., 2016;
63 Sherwen et al., 2016b). Recent studies have highlighted the importance of natural aerosols
64 originating from DMS oxidation and their contribution to the uncertainty of aerosol radiative
65 forcing in climate models (Carslaw et al., 2013; Fung et al., 2022; Rosati et al., 2022; Novak et al.,
66 2021, 2022). Since DMS-derived aerosol is a major source of uncertainty in estimating the global
67 natural aerosol burden and associated aerosol indirect radiative forcing, a more accurate
68 representation of DMS oxidation and particle formation processes is an important step towards
69 improved Earth system and climate modeling.

70 Although the chemistry of DMS oxidation has been previously studied in great detail, known
71 uncertainties and omissions in the current mechanism remain in current air quality and chemical
72 transport models (Barnes et al., 2006; Fung et al., 2022; Hoffmann et al., 2016, 2021). Furthermore,
73 while increasingly complex and experimentally validated mechanisms are under ongoing
74 development, DMS oxidation processes in many current chemical transport models continue to be
75 represented through simplified gas-phase reactions with the tropospheric oxidants OH and NO_3 ,
76 producing the two major oxidation products SO_2 and MSA at a fixed ratio as shown in R1-R3 in
77 Table 1 (Chen et al., 2018; Chin et al., 1996; Veres et al., 2020). This type of simplified mechanism
78 neglects the formation and loss of important intermediates such as dimethyl sulfoxide (DMSO:
79 CH_3SOCH_3), methane sulphinic acid (MSIA: $\text{CH}_3\text{SO}_2\text{H}$) and the recently discovered oxidation
80 product hydroperoxymethyl thioformate (HPMTF: $\text{HOOCH}_2\text{SCHO}$) (Berndt et al., 2019; Veres et
81 al., 2020; Wu et al., 2015; Khan et al., 2021).

82 These omissions can have major consequences on product yields of DMS oxidation, thereby
83 affecting the aerosol burdens. For example, the OH-addition pathway of DMS forms DMSO and
84 MSIA as the intermediates, which has been identified as a dominant source of MSA via their
85 aqueous-phase oxidation, and a fraction of that MSA subsequently undergoes aqueous-phase
86 oxidation to form sulfate aerosol (Chen et al., 2018; Ishino et al., 2021; Zhu et al., 2006; von
87 Glasow and Crutzen, 2004). Previous studies suggest that BrO contributes to 8 – 30% of total DMS

88 loss, highlighting the importance of this pathway as well (Breider et al., 2010; Boucher et al., 2003;
 89 Chen et al., 2018; Khan et al., 2016). More recent experimental and laboratory studies have
 90 confirmed the formation of methylthiomethyl peroxy radicals (CH₃CH₂OO; abbreviated as MSP
 91 or MTMP) from the H-abstraction channel of OH oxidation, which can subsequently lead to a
 92 series of rapid intramolecular H-shift isomerization reactions, ultimately resulting in the formation
 93 of the stable intermediate HPMTF (Berndt et al., 2019; Veres et al., 2020; Vermeuel et al., 2020;
 94 Wu et al., 2015; Fung et al., 2022; Jernigan et al., 2022a). It has been reported that 30–46% of
 95 emitted DMS forms HPMTF according to different modeling studies and this falls within the
 96 observational range from NASA Atmospheric Tomography ATom-3 and ATom-4 flight
 97 campaigns where about 30–40% DMS was oxidized to HPMTF along their flight tracks (Fung et
 98 al., 2022; Veres et al., 2020; Novak et al., 2021). Subsequent investigation of the isomerization
 99 rate and heterogeneous loss of HPMTF in cloud droplets and aerosol shows a high production rate
 100 of marine carbonyl sulfide (OCS) from the chemical loss of HPMTF, a potential precursor of
 101 stratospheric sulfate aerosol and significant inhibitor of cloud condensation nuclei (CCN)
 102 formation due to the resulting reduction of surface SO₂ (Jernigan et al., 2022a). With the latest
 103 experimental findings on heterogeneous loss process of HPMTF and experimentally validated
 104 oxidation reactions for OCS formation directly from HPMTF it is necessary to include these
 105 reactions as part of the DMS oxidation mechanism as these will have impact on overall yield of
 106 SO₂, thus affecting the formation probability of CCN (Jernigan et al., 2022a, b).
 107

Table 1. The three DMS oxidation reactions in the standard GEOS-Chem chemical mechanism

Reactions	Rate constant (cm ³ molecule ⁻¹ s ⁻¹)	
DMS + OH _(abstraction) → SO ₂ + CH ₃ O ₂ + CH ₂ O	1.20×10 ⁻¹¹ exp(-280/T)	(R1)
DMS + OH _(addition) → 0.75 SO ₂ + 0.25 MSA + CH ₃ O ₂	8.2×10 ⁻³⁹ [O ₂]exp(5376/T)/(1+1.05×10 ⁻⁵ ([O ₂]/[M]))	(R2)
DMS + NO ₃ → SO ₂ + HNO ₃ + CH ₃ O ₂ + CH ₂ O	1.90×10 ⁻¹³ exp(530/T)	(R3)

109
 110 Considering these and other consequences of complex DMS oxidation processes, a heavily
 111 simplified oxidation scheme will necessarily neglect potentially important reaction intermediates
 112 along with their production and loss pathways, with implications for the concentration and
 113 distribution of the oxidation products, including particulate sulfate. Differing intermediate
 114 lifetimes further influence sulfur removal and transport depending on the relative dominance of
 115 pathways. Thus, the exclusion of key pathways and intermediate species can lead to errors in the
 116 representation of the spatial distribution of both gas- and particle-phase sulfur species, as well as
 117 global sulfur burden.

118 The DMS oxidation products sulfate and MSA play an important role in Earth’s radiative budget
 119 through cloud droplet formation, and the extent of this role depends on how efficiently they can
 120 produce and grow new particles in the marine atmosphere (Thomas et al., 2010). SO₂ can oxidize
 121 in the gas-phase the forming H₂SO₄, which acts as a key product contributing to nucleation and
 122 condensational growth as shown in Figure 1. SO₂ oxidizing through aqueous chemistry in cloud
 123 droplets does contribute to particle growth rates by providing larger aerosol during cloud
 124 evaporation that acts as more efficient CCN (Kaufman and Tanré, 1994). On the other hand, MSA
 125 might participates in nucleation along with sulfuric acid in presence of amines or ammonia
 126 (Johnson and Jen, 2023). Recent studies have highlighted the importance of aqueous-phase
 127 chemistry in the formation and loss of MSA (Boniface et al., 2000; Chen et al., 2015; Kaufman
 128 and Tanré, 1994; Kulmala et al., 2000).

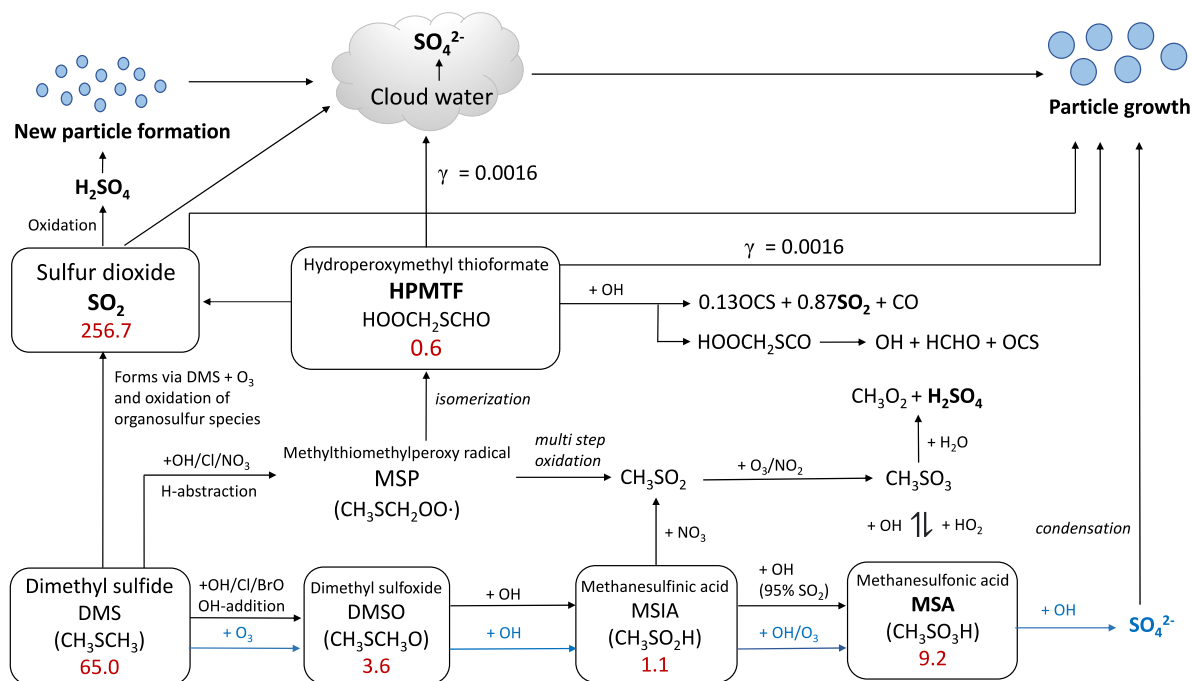


Figure 1 Modified DMS oxidation mechanism used in this work (simulation MOD) showing the formation of major stable oxidation products (in bold) including the newly identified intermediate HPMTF, and their contribution to new particle formation or growth of existing particles. The blue arrows and text represent aqueous-phase reactions. Numbers inside boxes indicate burden in units of GgS. γ values represent reactive uptake coefficients for heterogeneous loss of HPMTF to cloud and aerosol. Note that SO_2 formation from DMS and HPMTF involves multiple oxidation steps in this mechanism, but full pathways are simplified here for visual clarity

129 Additionally, the recently identified intermediate HPMTF also has the potential for further gas-
 130 phase oxidation. Under cloud-free conditions, HPMTF can undergo gas-phase oxidation by OH,
 131 producing SO_2 and eventually leading to the formation of non-sea-salt- SO_4^{2-} . This sulfate can
 132 contribute to aerosol formation and growth processes, with climate implications (Galí et al., 2019).
 133 Other work has used direct airborne eddy covariance flux measurements to explain the chemical
 134 fate of HPMTF in the MBL, finding that in cloudy conditions chemical loss due to aqueous phase
 135 reactions in clouds is the major HPMTF removal process (Novak et al., 2021). In the same study,
 136 global model simulations showed a 35% reduction in global annual average SO_2 production from
 137 DMS and a 24% reduction in the near-surface (0 to 3 km) global annual average SO_2
 138 concentrations over the ocean as a result of this process (Novak et al., 2021). Thus, a complete
 139 representation of cloud loss and aerosol uptake is needed to effectively evaluate the atmospheric
 140 impacts of marine DMS and their connections to cloud formation (Novak et al., 2021; Holmes et
 141 al., 2019).

142 To better understand the marine sulfur budget, as well as the eventual formation, size distribution,
 143 and seasonality of sulfate aerosol, we use the global chemical transport model GEOS-Chem,
 144 integrating previously developed mechanisms along with newly proposed pathways involving the
 145 formation and loss of the intermediates DMSO, MSIA, and HPMTF. As part of this work, we
 146 further quantify the atmospheric impacts of individual reactions and mechanisms, evaluate
 147 uncertainties in the chemical mechanism, and identify improvements necessary to better represent
 148 the impacts of DMS more accurately on atmospheric chemistry and climate. The resulting

149 integrated scheme provides a more complete representation of marine sulfur and sulfate aerosol
150 species in marine tropospheric environments compared to the simplified base GEOS-Chem
151 mechanism, with improved comparisons to aircraft and surface observations. Since aerosols are a
152 major contributor to uncertainty in climate forcing, improving oxidation and aerosol formation
153 mechanisms by adding and optimizing neglected reactions in models is a crucial step towards a
154 more mechanistically robust representation of particle yields and sensitivities. We further perform
155 multiple sensitivity tests to investigate how the uncertainty in heterogeneous uptake of the newly
156 identified HPMTF could influence DMS chemistry and tropospheric aerosol formation (Holmes
157 et al., 2019; Novak et al., 2021). In a broader sense our work provides a more detailed story on the
158 heterogeneous loss, fate, and ultimate impacts of DMS and its oxidation products, improving our
159 understanding of a key ocean-atmosphere interaction in the context of global change.

160 2 Methodology

161 To simulate DMS chemistry and its oxidation products GEOS-Chem global chemical transport
162 model v12.9.3 is used. Impacts on simulated aerosol size, number and mass concentration are
163 considered by coupling the Two-Moment Aerosol Sectional (TOMAS) aerosol microphysics
164 module with GEOS-Chem v12.9.3 (GC-TOMAS) (<https://github.com/geoschem/geos-chem/tree/12.9.3>) (Adams and Seinfeld, 2002; Kodros and Pierce, 2017). The default GEOS-Chem
165 chemical mechanism contains detailed HO_x-NO_x-VOC-O₃-halogen tropospheric chemistry
166 along with recently updated halogen chemistry and in-cloud processing (Bey et al., 2001; Holmes
167 et al., 2019; Chen et al., 2017; Parrella et al., 2012; Schmidt et al., 2016; Wang et al., 2019). The
168 DMS emission flux from ocean are controlled by a gas transfer velocity which is dependent on sea
169 surface temperature and wind speed (Johnson, 2010) and a climatology of concentrations in
170 seawater (Lana et al., 2011; Nightingale et al., 2000). The aqueous-phase concentration of O₃ in
171 aerosols or cloud droplets is calculated assuming gas-liquid equilibrium and aqueous-phase
172 concentration of OH is calculated following $[\text{OH}_{(\text{aq})}] = \delta[\text{OH}_{(\text{g})}]$ where, $\delta = 1 \times 10^{-19} \text{ M cm}^3$
173 molecule⁻¹ (Jacob et al., 2005; Chen et al., 2018).

175 In this study, TOMAS tracks aerosol number and the mass of each aerosol species in 15
176 logarithmically sized bins, with sizes in this analysis ranging from 3 nm to 10 μm (Lee and Adams,
177 2012; Lee et al., 2013). All binned aerosol species undergo interactive microphysics, allowing the
178 calculation of aerosol number budgets (Westervelt et al., 2013). The version of GC-TOMAS used
179 here includes 47 vertical levels, a horizontal resolution of 4° × 5°, and the GEOS-FP data product
180 for meteorological inputs. Simulations are performed for 2018, with 11 months of discarded model
181 spin up. Nucleation is simulated via a ternary nucleation scheme involving water, sulfuric acid,
182 and ammonia with nucleation rates scaled by 10⁻⁵ (Napari et al., 2002; Westervelt et al., 2013). In
183 low-ammonia regions (less than 1 pptv), a binary nucleation scheme involving water and sulfuric
184 acid is instead used (Vehkamäki et al., 2002). Previously GC-TOMAS has been used for aerosol
185 simulations to investigate topics such as the aerosol cloud-albedo effect and cloud condensation
186 nuclei formation (Kodros et al., 2016; Kodros and Pierce, 2017; Pierce and Adams, 2006;
187 Westervelt et al., 2013). Aerosol species available for GC-TOMAS simulations are sulfate, aerosol
188 water, black carbon, organic carbon, mineral dust, and sea salt (Alexander et al., 2005; Bey et al.,
189 2001; Duncan Fairlie et al., 2007; Pye et al., 2009). The wet and dry deposition scheme for aerosols
190 and gas species are based on previous studies (Amos et al., 2012; Emerson et al., 2020; Liu et al.,
191 2001; Wesely, 1989; Wang et al., 1998).

192 We refer to simulations performed using only these three DMS oxidation reactions (Table 1) as
193 the “BASE”, involving only the direct formation of SO₂ and MSA in gas-phase (Chin et al., 1996).
194 We further implement and evaluate a custom chemical mechanism for DMS oxidation, referred to
195 as “MOD” (Table 2-4), representing an integration of three individual DMS oxidation mechanism
196 updates explored previously using GEOS-Chem and CAM6-Chem. This mechanism also includes
197 HPMTF loss to clouds and aerosols via heterogeneous chemistry, dry and wet deposition of
198 HPMTF, along with further improvement based on recent literature updates to chemical kinetics
199 (Chen et al., 2018; Fung et al., 2022; Veres et al., 2020; Novak et al., 2021; Cala et al., 2023). In
200 GC-TOMAS we use specific subroutine that take amount of sulfate produced via in-cloud
201 oxidation and condense it into an existing aerosol size distribution. So, mass of sulfate produced
202 by oxidation is portioned to the various size bins according to the number of particles in that size
203 bin. TOMAS microphysics accounts for H₂SO₄ formation based on gas-phase oxidation of SO₂

204 included in the kinetic preprocessor (KPP) equation list valid for the simulation BASE. Since there
 205 are additional sources of sulfate in the integrated DMS oxidation mechanism both in gas and
 206 aqueous phase, we made necessary changes in the KPP code to explicitly track H₂SO₄ formation
 207 by gas phase oxidation of SO₂. On the other hand, code changes for sulfate formed by
 208 heterogeneous oxidation of MSA and HPMTF (in clouds and aerosols) were added in the GEOS-
 209 Chem microphysics module that also handles in-cloud oxidation of SO₂ in GC version 12.9.3 (Park
 210 et al., 2004; Trivitayanurak et al., 2008).

211 **Table 2.** Overview of the DMS oxidation mechanism via OH-addition pathway.

Gas-phase reactions	Rate constant (cm ³ molecule ⁻¹ s ⁻¹)	References
DMS + OH → DMSO + HO ₂	9.5×10 ⁻³⁹ [O ₂]exp(5270/T)/(1+ 7.5×10 ⁻²⁹ [O ₂]exp(5610/T))	IUPAC SOx22 (upd. 2006)
DMS + BrO → DMSO + Br	1.50×10 ⁻¹⁴ exp(1000/T)	(Bräuer et al., 2013; Hoffmann et al., 2016)
DMS + O ₃ → SO ₂	1.50×10 ⁻¹⁹	(Du et al., 2007; Burkholder et al., 2020)
DMSO + OH → 0.95(MSIA + CH ₃ O ₂)	6.10×10 ⁻¹² exp(800/T)	MCMv3.3.1, (von Glasow and Crutzen, 2004; Burkholder et al., 2020)
MSIA + OH → 0.95SO ₂ + 0.95CH ₃ O ₂	9.00×10 ⁻¹¹	MCMv3.3.1
MSIA + OH → 0.05MSA + 0.05HO ₂ + 0.05H ₂ O	9.00×10 ⁻¹¹	(von Glasow and Crutzen, 2004)
MSIA + NO ₃ → CH ₃ SO ₂ + HNO ₃	1.00×10 ⁻¹³	(von Glasow and Crutzen, 2004; Hoffmann et al., 2016)
Aqueous-phase reactions	k ₂₉₈ [M ⁻¹ s ⁻¹]	References
DMS (aq) + O ₃ (aq) → DMSO (aq) + O ₂ (aq)	8.61×10 ⁸	(Gershenson et al., 2001; Hoffmann et al., 2016)
DMSO (aq) + OH (aq) → MSIA (aq)	6.65×10 ⁹	(Zhu et al., 2003; Hoffmann et al., 2016)
MSIA (aq) + OH (aq) → MSA (aq)	6.00×10 ⁹	(Hoffmann et al., 2016; Herrmann et al., 1998)
MSI ⁻ (aq) + OH (aq) → MSA (aq)	1.20 × 10 ¹⁰	(Bardouki et al., 2002; Hoffmann et al., 2016)
MSIA (aq) + O ₃ (aq) → MSA (aq)	3.50×10 ⁷	(Hoffmann et al., 2016; Herrmann et al., 1998)
MSI ⁻ (aq) + O ₃ (aq) → MSA (aq)	2.00 × 10 ⁶	(Flyunt et al., 2001; Hoffmann et al., 2016)
MSA (aq) + OH (aq) → SO ₄ ²⁻	1.50×10 ⁷	(Hoffmann et al., 2016; Herrmann et al., 1998)
MS ⁻ (aq) + OH (aq) → SO ₄ ²⁻ (aq)	1.29 × 10 ⁷	(Zhu et al., 2003; Hoffmann et al., 2016)

212

213

214

Table 3. Overview of the DMS oxidation mechanism involving HPMTF formation.

Gas-phase reactions	Rate constant (cm ³ molecule ⁻¹ s ⁻¹)	References
MSP (CH ₃ SCH ₂ OO) → OOCH ₂ SCH ₂ OOH	2.2433×10 ¹¹ exp(- 9.8016e3/T)×(1.0348×10 ⁸ /T ³)	(Berndt et al., 2019; Veres et al., 2020; Wollesen de Jonge et al., 2021)
OOCH ₂ SCH ₂ OOH → HPMTF (HOOCH ₂ SCHO) + OH	6.0970×10 ¹¹ exp(- 9.489e3/T)×(1.1028×10 ⁸ /T ³)	(Berndt et al., 2019; Veres et al., 2020; Wollesen de Jonge et al., 2021)
OOCH ₂ SCH ₂ OOH + NO → HOOCH ₂ S + NO ₂ + HCHO	4.9×10 ⁻¹² exp(260/T)	MCMv3.3.1

MSP + HO ₂ → CH ₃ SCH ₂ OOH + O ₂	1.13×10 ⁻¹³ exp(1300/T)	MCMv3.3.1, (Wollesen de Jonge et al., 2021)
CH ₃ SCH ₂ OOH + OH → CH ₃ SCHO	7.03×10 ⁻¹¹	MCMv3.3.1
CH ₃ SCHO + OH → CH ₃ S + CO	1.11×10 ⁻¹¹	MCMv3.3.1
HPMTF + OH → HOOCH ₂ SCO + H ₂ O	4.00×10 ⁻¹²	(Jernigan et al., 2022a)
HPMTF + OH → 0.13OCS + 0.87SO ₂ + CO	1.40×10 ⁻¹¹	(Jernigan et al., 2022a)
OCS + OH → SO ₂	1.13×10 ⁻¹³ exp(1200/T)	(Jernigan et al., 2022a)
HOOCH ₂ SCO → HOOCH ₂ S + CO	9.2×10 ⁹ exp(-505.4/T)	(Wu et al., 2015)
HOOCH ₂ SCO → OH + HCHO + OCS	1.6×10 ⁷ exp(-1468.6/T)	(Wu et al., 2015)
HOOCH ₂ S + O ₃ → HOOCH ₂ SO + O ₂	1.15×10 ⁻¹² exp(430/T)	(Wu et al., 2015)
HOOCH ₂ S + NO ₂ → HOOCH ₂ SO + NO	6.0×10 ⁻¹¹ exp(240/T)	(Wu et al., 2015)
HOOCH ₂ SO + O ₃ → SO ₂ + HCHO + OH + O ₂	4.0×10 ⁻¹³	(Wu et al., 2015)
HOOCH ₂ SO + NO ₂ → SO ₂ + HCHO + OH + NO	1.2×10 ⁻¹¹	(Wu et al., 2015)

215
216

Table 4. Overview of the MSA-producing branch of the H-abstraction pathway of DMS oxidation.

Gas-phase reactions	Rate constant (cm ³ molecule ⁻¹ s ⁻¹)	References
DMS + OH → MSP (CH ₃ SCH ₂ OO) + H ₂ O	1.12×10 ⁻¹¹ exp(-250/T)	IUPAC SOx22 (upd. 2006)
DMS + Cl → 0.45MSP + 0.55C ₂ H ₆ SCl + 0.45HCl	3.60×10 ⁻¹⁰	(Fung et al., 2022; Enami et al., 2004)
C ₂ H ₆ SCl → DMSO + ClO	4.00×10 ⁻¹⁸	(Hoffmann et al., 2016; Urbanski and Wine, 1999)
DMS + NO ₃ → MSP + HNO ₃	1.9×10 ⁻¹³ exp(520/T)	MCMv3.3.1, (Novak et al., 2021; Wollesen de Jonge et al., 2021; Atkinson et al., 2004)
MSP + NO → CH ₃ SCH ₂ (O) + NO ₂	4.9×10 ⁻¹² exp(260/T)	MCMv3.3.1
MSP + MSP → 2HCHO + 2CH ₃ S	1.00×10 ⁻¹¹	(von Glasow and Crutzen, 2004)
CH ₃ SCH ₂ (O) → CH ₃ S + HCHO	1.0×10 ⁶	MCMv3.3.1
CH ₃ S + O ₃ → CH ₃ S(O)	1.15×10 ⁻¹² exp(430/T)	MCMv3.3.1; (Atkinson et al., 2004)
CH ₃ S + O ₂ → CH ₃ S(OO)	1.20×10 ⁻¹⁶ exp(1580/T)	MCMv3.3.1; (Atkinson et al., 2004)
CH ₃ S + NO ₂ → CH ₃ SO + NO	3.00×10 ⁻¹² exp(210/T)	IUPAC SOx60 (upd. 2006); (Atkinson et al., 2004)
CH ₃ S(O) + O ₃ → CH ₃ (O ₂) + SO ₂	4.00×10 ⁻¹³	IUPAC SOx61 (upd. 2006); (Borissenko et al., 2003)
CH ₃ SO + NO ₂ → 0.75CH ₃ SO ₂ + 0.75NO + 0.25SO ₂ + 0.25CH ₃ O ₂ + 0.25NO	1.20×10 ⁻¹¹	(Borissenko et al., 2003; Atkinson et al., 2004)
CH ₃ S(OO) → CH ₃ (O ₂) + SO ₂	5.60×10 ¹⁶ exp(-10870/T)	(Atkinson et al., 2004)
CH ₃ S(OO) → CH ₃ SO ₂	1.00	(Campolongo et al., 1999; Hoffmann et al., 2016)
CH ₃ S(OO) → CH ₃ S + O ₂	3.50×10 ¹⁰ exp(-3560/T)	MCMv3.3.1
CH ₃ SO ₂ + O ₃ → CH ₃ SO ₃ + O ₂	3.00×10 ⁻¹³	MCMv3.3.1; (von Glasow and Crutzen, 2004)
CH ₃ SO ₂ → CH ₃ (O ₂) + SO ₂	5.00×10 ¹³ exp(-9673/T)	MCMv3.3.1; (Barone et al., 1995)

$\text{CH}_3\text{SO}_2 + \text{NO}_2 \rightarrow \text{CH}_3\text{SO}_3 + \text{NO}$	2.20×10^{-11}	(Atkinson et al., 2004)
$\text{CH}_3\text{SO}_3 + \text{HO}_2 \rightarrow \text{MSA}$	5.00×10^{-11}	MCMv3.3.1; (von Glasow and Crutzen, 2004)
$\text{CH}_3\text{SO}_3 \rightarrow \text{CH}_3(\text{O}_2) + \text{H}_2\text{SO}_4$	$5.00 \times 10^{13} \exp(-9946/T)$	MCMv3.3.1
$\text{MSA} + \text{OH} \rightarrow \text{CH}_3\text{SO}_3$	2.24×10^{-14}	MCMv3.3.1

217 To examine the sensitivities of size-resolved aerosol formation and growth to DMS chemistry
 218 modifications, model simulations are conducted as summarized in Table 5. Output from
 219 simulations MOD and MOD_noHetLossHPMTF was then compared against simulation BASE to
 220 understand the contribution of these additional chemical reactions on spatial pattern of the surface
 221 concentration of major oxidation products of DMS.

222 **Table 5.** List of mechanisms used in GEOS-Chem-TOMAS simulations.

Model Runs	Mechanism	HPMTF Cloud Loss*	HPMTF Aerosol Loss*
BASE	All reactions from Table 1	-	-
MOD_noHetLossHPMTF	All reactions from Table 2-4	Off	Off
MOD	All reactions from Table 2-4	On	On

223 * Instantaneous formation of sulfate via HPMTF cloud and aerosol loss uses a reactive uptake co-efficient (γ) of
 224 0.0016.

225 As shown in Table 2, the modified DMS chemistry simulations examined here include gas- and
 226 aqueous-phase oxidation of DMS and its intermediate oxidation products by OH, NO₃, O₃, and
 227 halogenated species as previously explored in an older version of GEOS-Chem (Chen et al., 2018).
 228 The aqueous-phase reactions in cloud droplets and aerosols were parameterized assuming a first-
 229 order loss of the gas-phase sulfur species (Chen et al., 2018). Further building upon this previous
 230 mechanism, the scheme used here also includes the formation and loss of HPMTF as previously
 231 tested in the global climate model CAM6-Chem as shown in Table 3 (Veres et al., 2020). Table 4
 232 presents the third piece of the mechanism: a gas-phase MSA-producing branch of the H-abstraction
 233 pathway in the DMS chemistry bridging the other two sets of the reactions (Fung et al., 2022). To
 234 avoid addition of SO₃ oxidation chemistry we have replaced SO₃ with H₂SO₄ followed by previous
 235 work for the decomposition reaction of CH₃SO₃ (Table 4). A similarly integrated mechanism
 236 (Table 2-4) has been previously explored using the CAM6-Chem model with a focus on radiation
 237 budget impacts, which is improved in this work through updates rate constants and the inclusion
 238 of additional relevant reactions (Fung et al., 2022; Novak et al., 2021; Wollesen de Jonge et al.,
 239 2021; Cala et al., 2023). The newly added reactions and their respective rate constants are largely
 240 based on the MCMv3.3.1 and the literature cited in the Table 2-4 reference list. We use a rate
 241 constant of $1.40 \times 10^{-11} \text{ cm}^3 \text{ molecules}^{-1} \text{ s}^{-1}$ for HPMTF + OH, which was previously determined
 242 based concentrations of other known sulfur species (DMS, DMSO, SO₂ and methyl thioformate;
 243 MTF; CH₃SCHO; a structurally similar proxy to HPMTF) and evaluated by box model (Jernigan
 244 et al., 2022a). An exploration of reaction rate uncertainty for the HPMTF+OH reaction (Table 3),
 245 including both high and low end limits of $5.5 \times 10^{-11} \text{ cm}^3 \text{ molecules}^{-1} \text{ s}^{-1}$ and $1.4 \times$
 246 $10^{-12} \text{ cm}^3 \text{ molecules}^{-1} \text{ s}^{-1}$ resulted in only minor impacts on the fate of HPMTF and ultimate sulfate
 247 formation in our simulations (Novak et al., 2021; Wu et al., 2015).

248 Model sensitivity simulations were also performed with (case “MOD”) and without HPMTF
 249 heterogeneous uptake to clouds and aerosols (case “MOD_noHetLossHPMTF”) to account for
 250 how much of the DMS-derived HPMTF eventually forms SO₂ in the presence of these additional
 251 loss processes (Table 5). Previous work shows that aerosol surface chemistry causes additional

252 decreases in HPMTF mixing ratios, primarily over land, and that the loss of HPMTF in clouds is
253 larger (36%) than losses from aerosols (15%) when using an uptake coefficient of $\gamma = 0.01$ for both
254 processes (Novak et al., 2021). In this work, based on recent laboratory measurements, we use a
255 smaller uptake coefficient ($\gamma = 0.0016$) for HPMTF loss to aerosols and clouds (Table 5) (Jernigan
256 et al., 2022b). We assume HPMTF directly produces sulfate in cloud and aerosol followed but
257 previous work even though there is uncertainty in the fate of HPMTF heterogeneous loss (Zhang
258 and Millero, 1993; Novak et al., 2021; Jernigan et al., 2022a). For the aqueous-phase reactions
259 listed in Table 2, including the oxidation of intermediates DMSO and MSIA in cloud droplets and
260 aerosols, a first-order loss of the gas-phase sulfur species was assumed following previously used
261 parameterizations and physical parameter values (Chen et al., 2018). Alongside the gas-phase and
262 aqueous-phase reactions relevant to the added DMS oxidation mechanism contributing to the
263 formation of SO₂ and sulfate, the default version of GC-TOMAS used here also includes in-cloud
264 oxidation of SO₂ by H₂O₂, O₃, and O₂ catalyzed by transition metals (Mn, Fe), as well as the loss
265 of dissolved SO₂ by HOBr and HOCl, all of which are passed to TOMAS to account for sulfate
266 production (Chen et al., 2017; Wang et al., 2021).

267 All simulations are conducted for the year 2018, which was chosen to match the model simulation
268 with the dates of the NASA Atmospheric Tomography flight campaign (ATom-4) offering
269 observational data for HPMTF, DMS and SO₂. Rate coefficients for all gas-phase sulfur reactions
270 are obtained from the most recent JPL report and other references while sulfur product yields for
271 gas-phase reactions are obtained from various laboratory and modeling studies (Burkholder et al.,
272 2020; Lucas and Prinn, 2002; Hoffmann et al., 2016; Gershenson et al., 2001; Kowalczyk et al.,
273 2003; Zhou et al., 2019; Jernigan et al., 2022a). The simulations included sea salt debromination
274 except for some sensitivity tests described below (Zhu et al., 2019; Schmidt et al., 2016). In all our
275 simulations including MOD, DMS is advected and undergoes chemical loss and transport but does
276 not undergo dry or wet deposition. However, dry and wet deposition of oxidation products such as
277 DMSO, MSIA, MSA and HPMTF are included.

278 We note that previous work has explored the impact of MSA on aerosol growth, including
279 modifications within TOMAS to represent this process (Hodshire et al., 2019). We do not include
280 this process here. Future work is recommended to examine its importance in the context of the
281 chemistry updates presented here.

282 **3 Result and discussion**

283 3.1 Model-Observations Comparison

284 3.1.1 Surface DMS mixing ratio

285 We compared the modeled DMS mixing ratio averaged for each month with the observational data
286 collected at Crete Island (35° N, 26° E) and Amsterdam Island (37° S, 77° E) (Kouvarakis and
287 Mihalopoulos, 2002; Chen et al., 2018; Castebrunet et al., 2009). Comparing simulations BASE
288 and MOD, we find a closer match with DMS observations for simulations using modified DMS
289 chemistry for both observation data shown in Figure 2. Modeled DMS mixing ratios calculated
290 using base chemistry show strong positive bias during the months of May and June for Crete
291 Island. By comparison, during the same period the modeled DMS mixing ratios calculated with
292 modified chemistry reduces the bias from 102% to 42%. Similarly, for Amsterdam Island major
293 overpredictions are apparent for the BASE simulation compared to MOD for the months of May-
294 August. One reaction that may play a role in this shift is DMS + BrO, which as indicated earlier is
295 responsible for a faster overall chemical loss of DMS, in particular over the southern hemisphere
296 high latitudes. Beside DMS chemistry, sea surface DMS concentration is also proven to affect the
297 modeled DMS mixing ratio (Chen et al., 2018). But the aim of this study is to investigate the
298 chemistry aspect of DMS oxidation, so we did not explore how change in DMS seawater
299 climatology and thus their emission influence the surface DMS mixing ratio.

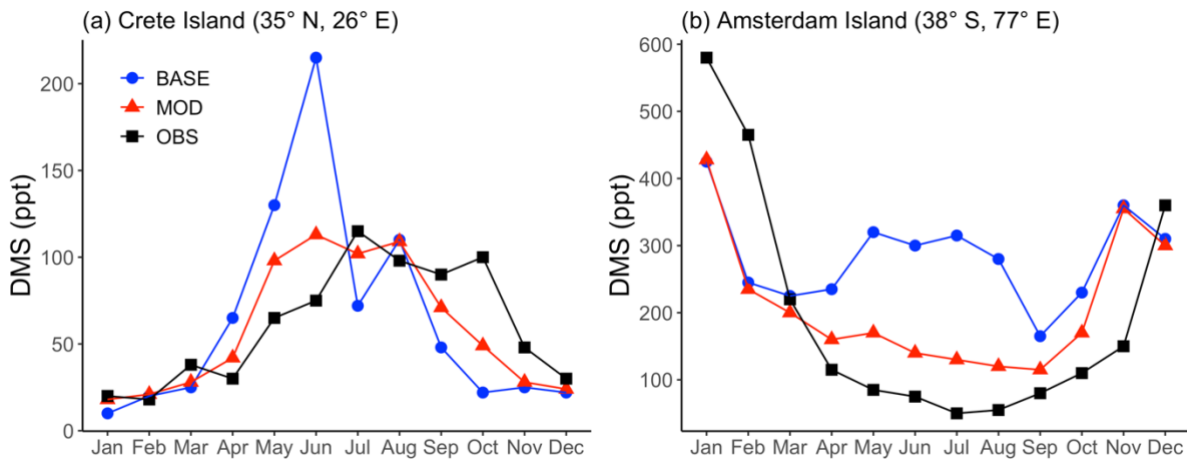


Figure 2 Observed (OBS) monthly mean surface DMS mixing ratios at (a) Crete Island and (b) Amsterdam Island compared with simulations BASE and MOD. Simulations are described in Table 5.

300

301 3.1.2 Comparison with aircraft observations

302 We further evaluate model output through a comparison with ATom-4 aircraft observations for
303 specific days of measurement for DMS, HPMTF and SO₂ as shown in Figure 5. For this
304 comparison, the model is sampled at the time and location of aircraft measurements by ATom-4
305 using the planeflight diagnostic of GEOS-Chem.

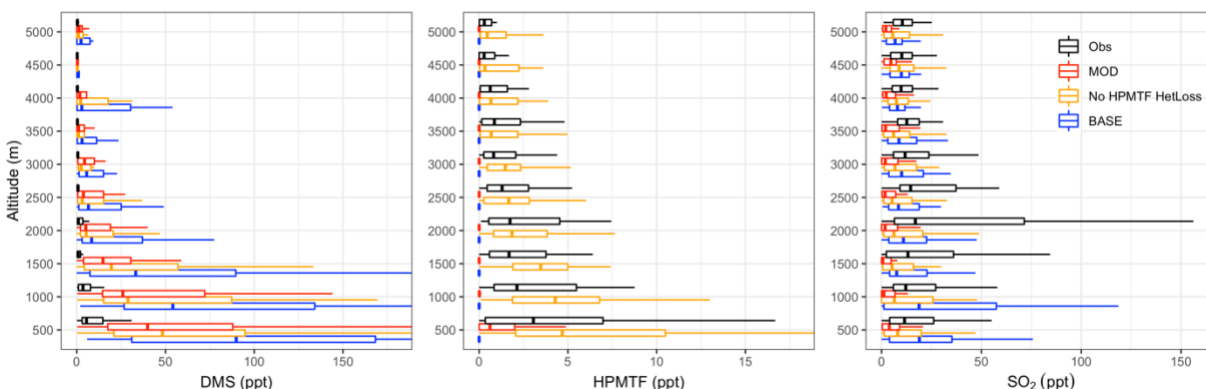


Figure 3 Vertical profiles of (a) DMS, (b) HPMTF and (c) SO_2 mixing ratios from ATom-4 observations (black) and model with simulation MOD sampled along the ATom-4 flight tracks (red) binned every 500 m of flight altitude. Also shown are modeled results without HPMTF heterogeneous loss with simulation MOD_noHetLossHPMTF (yellow), and for BASE GEOS-Chem chemistry (blue). Box plot whiskers show full range of distribution at each altitude bin. DMS observations are from Whole Air Samples (WAS) while HPMTF DC-8 observations are from iodide ion chemical ionization time-of-flight mass spectrometer (CIMS). SO_2 observations from ATom-4 campaign were measured by Laser Induced Fluorescence (LIF).

306 DMS concentrations measured during ATom-4 by whole air sampler (WAS) and modified
 307 chemistry simulation values for nearest neighbor grid cells are shown in Figure 3a across different
 308 altitude. In general, the modeled DMS concentrations are significantly higher than those observed
 309 during ATom-4 missions especially close to the surface. However, model DMS concentrations
 310 decrease more rapidly than the measurement with altitudes indicating vertical mixing could be one
 311 of the underlying reasons for this trend. Even with this near surface bias, simulation MOD relative
 312 to BASE has greater DMS losses and a shorter DMS lifetime (from 1.5 d to 0.9 d) reducing the
 313 gap between modeled and observed concentration compared to simulation BASE. The reduction
 314 in modeled DMS is largest over the Southern Ocean (shown later in Fig. 5b) where oxidation by
 315 BrO and O_3 in the aqueous phase plays the major role in reducing DMS concentration, thereby
 316 reducing the model-observation bias (Fig. 3b). Remaining model biases could be at least partially
 317 attributed to model uncertainty in oxidant concentrations and cloud cover. The heterogeneous loss
 318 of HPMTF has minimal impact on DMS concentration and its vertical profile.

319 For HPMTF, Figure 3b shows that the observed and modeled HPMTF concentrations remain
 320 largely below 15 ppt. Agreement between observations and modeled HPMTF mixing ratios in the
 321 vertical profile (Fig. 3b) is poor for simulation MOD even close to the surface. Removing all
 322 heterogeneous loss of HPMTF improves model comparisons aloft, though surface concentrations
 323 become overestimated (yellow line of Fig. 3b), showing a high sensitivity to cloud and aerosol
 324 loss processes. We also find that the modeled HPMTF:DMS ratios range from 0.15:1 to 0.5:1 on
 325 a daily basis in most cases for when there is no heterogeneous loss of HPMTF, compared to 0.5:1
 326 observed during ATom-4 using the calibration maintained during measurement, implying
 327 reasonably good agreement for this value over daily time scales (Veres et al., 2020). The SARP
 328 flight campaign data has reported much lower HPMTF:DMS ratios (< 0.2) on cloudy days which
 329 is relatable to modeled HPMTF with simulation MOD (Novak et al., 2021). For simulation MOD,
 330 the modeled HPMTF:DMS ratio is 0.03:1 for until 0.5 km and then approaches zero with
 331 increasing altitude, indicating the need for additional work to better constrain production and loss
 332 processes of this intermediate. Our simulations indicate that cloud loss is the dominant modeled
 333 removal process of HPMTF, consistent with previous findings, while gas-phase OH oxidation

334 plays a minor role (Novak et al., 2021). Thus, the addition of cloud uptake dramatically decreases
335 HPMTF concentrations throughout the troposphere. Overall, this allows only 10% of HPMTF
336 produced to end up as SO₂ with about 89% lost to clouds and aerosol and thus removed from the
337 system, resulting net reduction in mean global SO₂ by about 40% along with other chemical
338 processes involved for this reduction as well. Previous work focusing entirely on gas-phase and
339 heterogeneous loss of HPMTF shows a much higher bias for both DMS and HPMTF during cloudy
340 and clear sky conditions using the same model and a condensed DMS oxidation mechanism,
341 indicating that the addition of gas-phase and heterogeneous oxidation of DMS including additional
342 intermediates such as DMSO and MSIA further reduce model biases for HPMTF with remaining
343 overestimation of the multiphase loss for HPMTF (Novak et al., 2021).

344 We also compared the SO₂ concentrations measured during ATom-4 by Laser Induced
345 Fluorescence (LIF) and simulation MOD values for nearest neighbor grid cells are shown in Figure
346 3c across different altitude. Modeled surface SO₂ concentrations are lower than those observed
347 during ATom-4 missions across the vertical scale shown here for simulation MOD. The greater
348 SO₂ losses results in a shorter SO₂ lifetime (from 1.4 d to 1.3 d) for simulation MOD relative to
349 simulation BASE. The reduction in modeled SO₂ is largest over the Southern Ocean (shown later
350 in Fig. 7a) where heterogeneous oxidation of HPMTF is most efficient and irreversible. Besides,
351 the OH addition channel of DMS does not directly produce SO₂ causing further reduction in the
352 concentration relative to BASE. Removing the heterogeneous loss of HPMTF increases the
353 modeled SO₂ compared to simulation MOD with underprediction remaining. Remaining model
354 biases could be at least partially attributed to uncertainty in DMS oxidation processes along with
355 other non-DMS sources contributing high concentration of SO₂. Aside from uncertainty in DMS
356 emissions and oxidation, recent understanding of marine sulfur chemistry such as methanethiol
357 (CH₃SH) oxidation has been reported as a significant source of SO₂ in the marine atmosphere
358 and could help reduce the bias, a possibility deserving further investigation (Berndt et al., 2023;
359 Novak et al., 2022). Overall the DMS oxidation chemistry implemented in this work reduces the
360 model observation bias close to the surface (up to 1km) compared to BASE GEOS-Chem
361 chemistry.

362 Besides the vertical profile shown in Figure 3b, the global mean surface mixing ratio of HPMTF
363 with simulation MOD_noHetLossHPMTF for May 2018 is plotted in Figure 4 and compared with
364 the observational measurement of HPMTF made during the ATom-4 mission during the NASA
365 DC-8 flight campaign, which sampled the daytime remote marine atmosphere over the Pacific and
366 Atlantic Oceans. The ATom-4 measurements were carried out during daytime hours between April
367 24 and May 21, 2018 for 21 non-continuous days.

368 For this campaign, flight patterns covered vertical profiles from 0.2 to 14 km above the ocean
369 surface. The flight leg duration was 5 minutes and boundary layer altitude of 150 to 200 m above
370 the ocean surface. Since most of these measurement days are within the month of May 2018, here
371 we compare observations with modeled output of mean surface concentration of HPMTF for this
372 month. With the rate of isomerization reaction used in previous work, we find spatial patterns of
373 monthly mean surface concentrations are generally well captured (Jernigan et al., 2022a). Overall,
374 we find that the simulation MOD_noHetLossHPMTF results in better agreement with existing
375 overprediction for the vertical profile (Fig. 3b) and global surface layer HPMTF levels (Fig. 4)
376 compared to previous modeled approaches using the CAM-chem model (Veres et al., 2020).

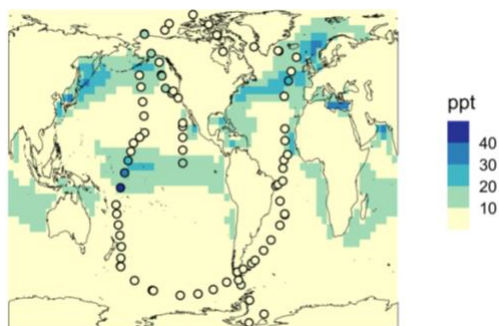


Figure 4 Geographic distribution of May 2018 monthly mean surface-layer mixing ratio of HPMTF for simulation MOD_noHetLossHPMTF mechanism represented for May 2018. The circles represent measurements of HPMTF during the ATom-4 mission by NASA DC-8 flight tracks with a limit of detection <1 ppt.

377

378 3.2 DMS burden and oxidation pathways

379 We find that the global burden of DMS in the MOD simulation is 65 Gg S (Table B1), 40% lower
 380 than what we find with the simulation BASE (108 Gg S). Even with this 42% reduction, global
 381 burdens are still well within the range of 9.6–150 Gg S suggested in other studies (Faloon, 2009;
 382 Kloster et al., 2006). Figure 5a shows that surface DMS mixing ratios are highest in the North
 383 Pacific and North Atlantic oceans for June-July-August (JJA) and in the Southern Ocean during
 384 the months of December-January-February (DJF), revealing the underlying seasonality of DMS
 385 emissions. According to previous studies, the highest DMS concentrations usually occur in
 386 summer months due to higher rates of primary production in the presence of adequate solar
 387 irradiation and high temperatures for both hemisphere (Galí et al., 2018; Lana et al., 2011; Wang
 388 et al., 2020). In simulation MOD, the global mean surface-layer DMS burden was higher in SH
 389 for DJF and lower in NH for JJA which is due to larger ocean area in the SH than NH. We also
 390 find that the reactions of this expanded DMS oxidation mechanism collectively contribute to
 391 reductions in mean surface-layer DMS concentration of 58% and 22% compared to BASE for JJA
 392 and DJF respectively (Fig. 5b). These reductions are due primarily to the addition of multiple new
 393 chemical loss pathways compared to BASE, which are especially impactful during JJA months
 394 due to elevated BrO in the SH winter and also higher O₃ and OH concentration in the NH
 395 summer compared to the SH summer (Zhang et al., 2018; Pound et al., 2020).

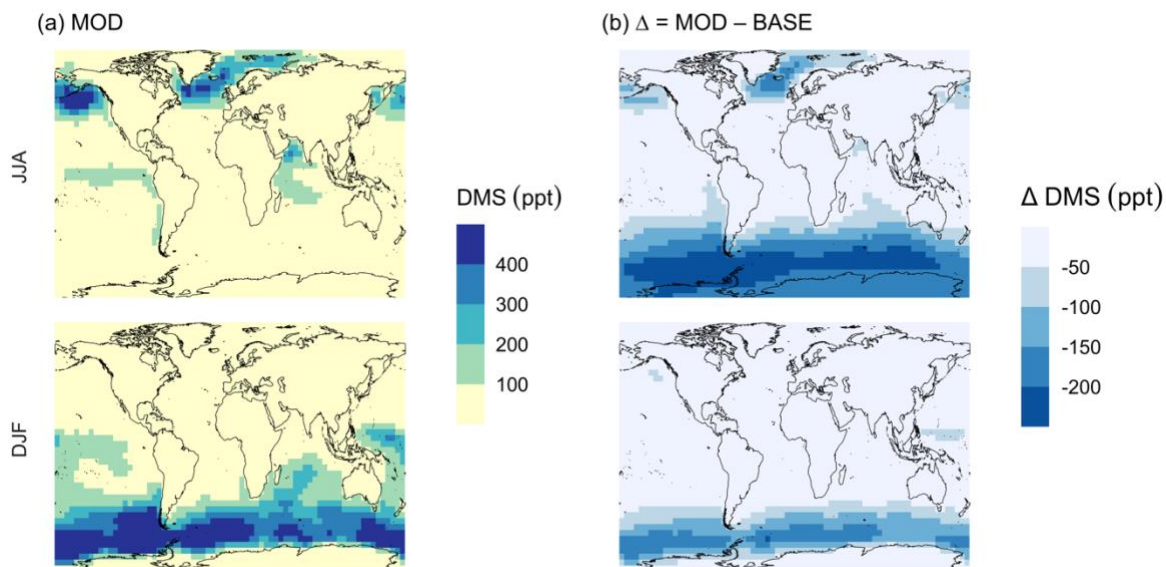


Figure 5 Geographic distribution of mean surface DMS mixing ratio (ppt) for simulation (a) MOD and (b) difference between simulations from its baseline, $\Delta = \text{MOD} - \text{BASE}$ from GEOS-Chem simulations. Here, JJA and DJF represent June-July-August and December-January-February respectively. Simulations are described in Table 5.

396 As shown in Fig. 5b, this DJF DMS reduction is seen mainly over the Southern Ocean and is
 397 largely attributable to faster chemical losses through the added reactions of $\text{DMS} + \text{BrO}$ and
 398 $\text{DMS}_{(\text{aq})} + \text{O}_{3(\text{aq})}$, which in earlier work was hypothesized as a possible reason for high model biases
 399 in the absence of detailed halogen chemistry (Chen et al., 2016). The global lifetime of DMS
 400 decreases from 1.5 days in the BASE simulation to 0.9 day in the MOD simulation.

401 These values are comparable to the range of 0.8–2.1 d reported by previous studies (Chen et al.,
 402 2018; Fung et al., 2022). The global DMS emission flux (F_{DMS}) from ocean to the atmosphere is
 403 22 Tg S yr^{-1} and is within the range of 11– 28 Tg S yr^{-1} simulated by GEOS-Chem and other
 404 models in previous studies (Lennartz et al., 2015; Fung et al., 2022; Chen et al., 2018; Hezel et al.,
 405 2011; Spracklen et al., 2005). Our F_{DMS} is higher than the 18 Tg S yr^{-1} which uses sea surface
 406 DMS concentration from Kettle et al. (1999) as reported (Chen et al., 2018) indicating the DMS
 407 emission varies with change in sea surface DMS climatology. The analysis and improvement of
 408 DMS emissions directly is not a part of this work, but we note that improved and validated
 409 inventories for DMS will certainly play a role in subsequent oxidation product comparisons. We
 410 recommend ongoing evaluation of DMS emissions inputs to complement the expanded chemical
 411 mechanism development we present here.

412 In the BASE simulation the chemical loss of DMS acts as its only sink (as opposed to dry and wet
 413 deposition), leading to a full conversion yield of DMS into SO_2 (82.5%) and MSA (17.5%) (Fig.
 414 A3a). Figure 6 shows that in simulation MOD with updated DMS oxidation scheme DMS is
 415 mainly oxidized by OH in the gas phase, with 27.6% of losses proceeding via the H-abstraction
 416 channel and 38.6% via the OH-addition pathway, together contributing up to 66.2% of global
 417 average loss with high regional contribution over the tropical oceans via the abstraction channel
 418 where surface OH is the highest. NO_3 oxidation of DMS accounts for another 11.2% of global
 419 DMS chemical losses, comparable to values found in previous studies (Chen et al., 2018; Fung et

420 al., 2022). Over the ocean, the NO_3 loss pathway is strongest in the NH coastal regions due to
421 outflow of NO_x sources from over the land whereas for the SH values are generally less than 10%.
422 Oxidation by BrO is responsible for 18.4% of the global DMS removal, falling within the
423 previously estimated range of 8%–29% (Boucher et al., 2003; Khan et al., 2016; Chen et al., 2018).
424 Regionally, its contribution can reach 50%–60% over high latitudes of the Southern Hemisphere
425 as well as to the north near the Arctic Ocean, consistent with previous box model studies based on
426 the availability of high BrO and low OH and NO_3 for those regions (Hoffmann et al., 2016). DMS
427 + O_3 accounts for 2.2% (aqueous) and 0.9% (gas phase) of global surface DMS loss. The higher
428 contribution from BrO and lower from O_3 using this mechanism compared to some previous
429 studies could be explained in part by the recently implemented sea-salt debromination mechanism
430 in GEOS-Chem, resulting in a much higher background level of BrO as well as lower O_3
431 abundance, especially in the southern hemisphere (Boucher et al., 2003; Chen et al., 2018; Fung
432 et al., 2022; Sherwen et al., 2016a; Wang et al., 2021). To further quantify the importance of the
433 sea salt debromination mechanism, we perform an emissions sensitivity test by turning this
434 emission source off while using updated MOD chemistry (Fig. A1). As would be expected, these
435 simulations show much lower BrO formation (as shown in Fig. A6) and resulting chemical
436 impacts, with overall oxidation contributions comparable to previous literature (Schmidt et al.,
437 2016; Wang et al., 2021). We find that under this scenario the relative contribution of BrO for
438 DMS loss decreases to 2.2%, while the DMS + O_3 pathway increases to 43.3% (aqueous) and 1.4%
439 (gas phase), and the DMS + OH pathway increases to 31.0% (abstraction) and 48.0% (addition)
440 of global surface DMS loss (Fig. A1). The DMS loss via interaction with NO_3 also increases to
441 2.0% when sea salt debromination is turned off in the mechanism. The relative contributions of
442 other oxidants remain mostly unaffected in the BrO sensitivity test.

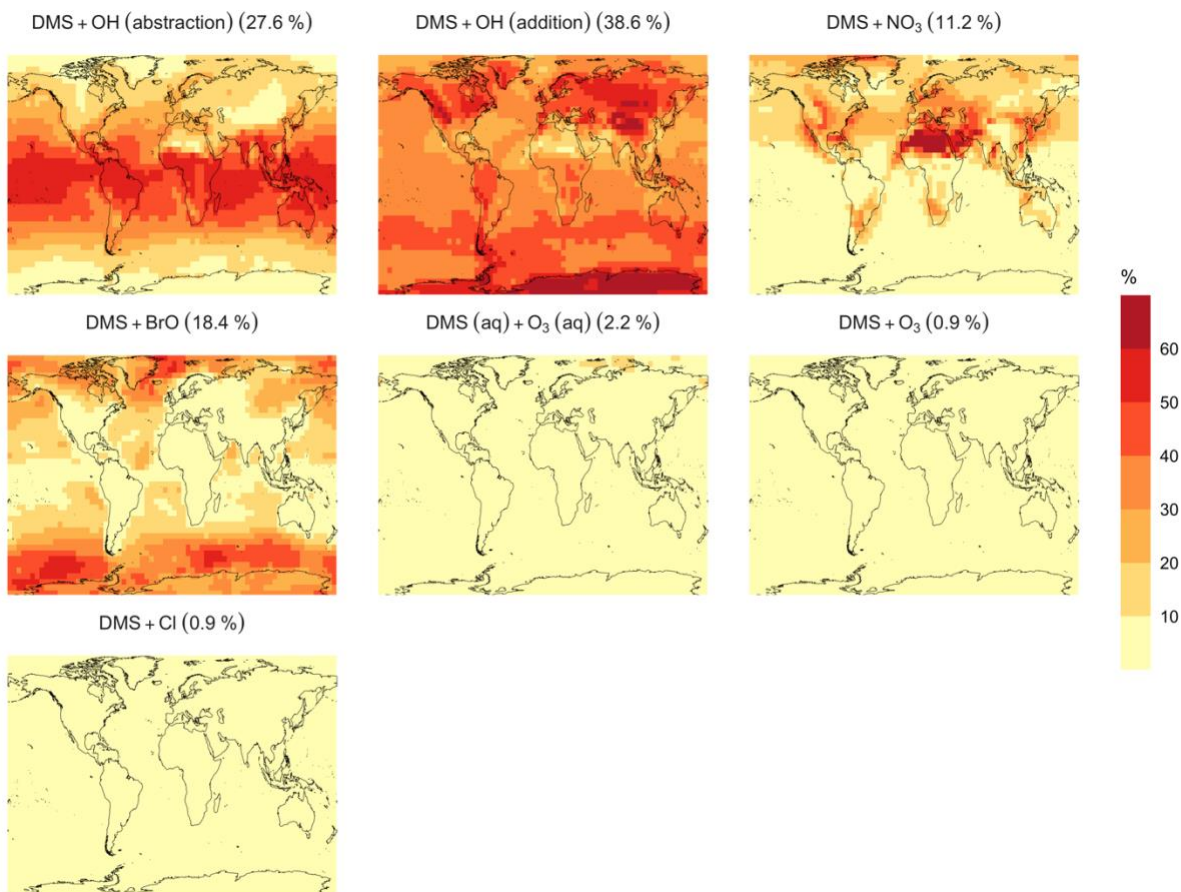


Figure 6 Geographic distribution of the annual mean surface layer fraction of total DMS oxidation (percent) attributed to different tropospheric oxidants for simulation MOD (described in Table 5). Percentages in parentheses indicate the average contribution to global chemical loss for the fraction of DMS emitted for each reaction pathways presented here.

443 Regionally, the fractional contribution of aqueous-phase DMS + O₃ to DMS oxidation can be up
 444 to 10%–20% over high-latitude oceans especially with the sea salt debromination is turned off
 445 (Fig. A1), which is in the middle of the 5%–30% contribution to high-latitude DMS losses
 446 previously reported (Chen et al., 2018; Fung et al., 2022; von Glasow and Crutzen, 2004). The Cl
 447 oxidation reaction contribute about 0.9% for with and without sea salt debromination to the
 448 chemical removal of DMS, consistent with some previous studies (Atkinson et al., 2004; Fung et
 449 al., 2022). This does differ from other reported values however, including those from a global
 450 model study (4%) and box model simulations (8%–18%) (Chen et al., 2018; Hoffmann et al.,
 451 2016; von Glasow and Crutzen, 2004). It's worth noting that none of the studies reporting such
 452 high Cl contributions included HPMTF formation and loss. Ongoing uncertainties associated with
 453 model-observation bias of Cl should be further resolved to get better representation of halogenated
 454 species contributions to DMS loss (Wang et al., 2021). Due to slower reaction kinetics and lower
 455 fractional contribution reported earlier compared to BrO with DMS and uncertainty in surface
 456 concentration and kinetics for photochemically generated halogenated species such as Br, IO we
 457 did not include them in our chemical scheme (Chen et al., 2018).

458 3.3 Implications of the extended DMS oxidation mechanism

459 Figure 7 shows that the MOD simulation results in 40% reduction of surface layer SO₂ relative to
 460 BASE, but a huge increase in SO₄²⁻ in most regions. These changes suggest that the combination
 461 of gas-phase and aqueous-phase reactions results in a higher net yield of MSA and HPMTF and a
 462 lower net yield of gas-phase SO₂. Additionally, comparison of simulation MOD relative to
 463 MOD_noHetLossHPMTF (Fig. A2a) shows that loss of HPMTF in cloud droplets and aerosol
 464 reduces the global mean production of SO₂ by 21.4%, contributing to the SO₂ reduction and
 465 increasing mean surface layer sulfate by 12.4% (Fig. A2b). This reduction in SO₂ is expected to
 466 reduce the availability of gas-phase sulfuric acid for new particle formation by nucleation (Clarke
 467 et al., 1998a). Total SO₄²⁻ increases over the ocean, however, because the increased SO₄²⁻
 468 production from rapid loss of MSA and HPMTF in aqueous-phase offsets the reduced oxidation
 469 of SO₂ (Fig. 7b). In addition to that, reduced gas-phase sulfur species such as CH₃SO₃ also
 470 contribute to sulfate formation in our mechanism as followed by other works (Fung et al., 2022).
 471

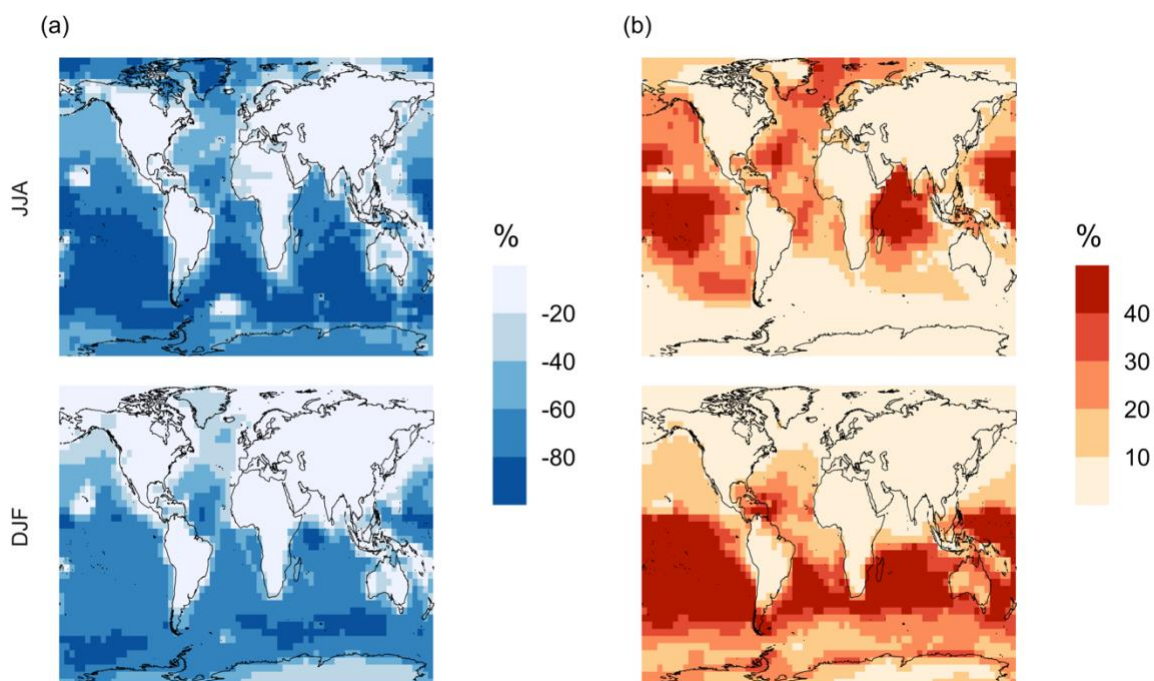


Figure 7 Percent change in simulated surface layer (a) SO₂ and (b) SO₄²⁻ for simulation MOD relative to BASE for June, July and August mean (JJA) and December, January, and February mean (DJF). Simulations are described in Table 5.

472 Qualitatively, the regions showing the highest percent changes of SO₂ are consistent with previous
 473 studies that included HPMTF chemistry and loss processes though the extent of this reduction is
 474 much higher with the integrated mechanism used in our study (Fig. 7a) (Novak et al., 2021). The
 475 regions with the largest percent change in SO₂ reduction are those where DMS oxidation
 476 contributes most to SO₂, and where HPMTF production and in-cloud oxidation of HPMTF are
 477 efficient. This spatial pattern thus helps us to identify where the production and heterogeneous loss
 478 of HPMTF and MSA is enhanced. One of the reactions that possibly contributes to delayed
 479 formation and reduction of SO₂ concentration is the first-generation OCS formation from OH
 480 oxidation of HPMTF. We find that addition of cloud and aerosol loss significantly decreases the
 481 OCS production, especially in high cloud cover regions as previously reported (Jernigan et al.,

482 2022a). Even though the cloud loss of HPMTF increases the production of surface sulfate, the total
 483 global sulfate burden we calculate increases by only 6.5% from the BASE sulfate burden of around
 484 575 Gg S. This can be attributed to minor contribution of DMS and its intermediate oxidation
 485 products in SO₂ production compared to other non-DMS derived sources. In addition, the
 486 production of stable intermediate oxidation products delay the conversion of SO₂ to SO₄²⁻ and
 487 modify its spatial distribution in the marine environment. Thus, we should expect these aqueous
 488 phase oxidation products to contribute to particle mass rather than increase the number of nucleated
 489 particles, as suggested in other studies (Clarke et al., 1998b; Novak et al., 2021; Williamson et al.,
 490 2019).
 491

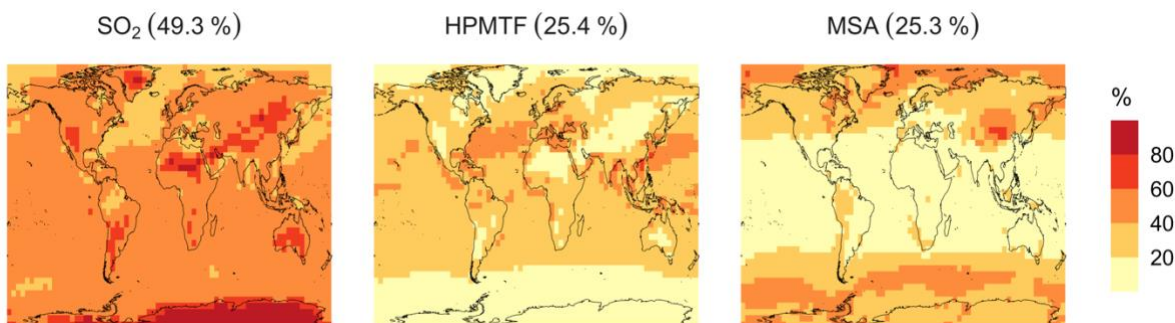


Figure 8 Simulated branching ratio (in %) of the DMS oxidation mechanism considering SO₂, HPMTF and MSA as major terminal oxidation products calculated from their annual total production rate for simulation MOD.

492 The spatial distribution of product branching ratios of DMS oxidation is shown in Figure 8. Here,
 493 25.4% of the annual total DMS oxidation will end up as HPMTF, while final SO₂ yield decreases
 494 to 49.3% compared to 82.5% for the BASE simulation (Fig. A3a). The terminal HPMTF branch
 495 represents sulfur removed from the system by cloud and aerosol uptake of HPMTF, leading to a
 496 reduced overall formation of SO₂. With sea salt debromination turned off, modified chemistry
 497 forms even more HPMTF (27.7%), slightly higher SO₂ (51.3%), and lowers the yield of MSA to
 498 21.0% (25.3% with the sea salt debromination on), underscoring the importance of halogen
 499 chemistry for MSA production (Fig. A3b). These results are comparable with observationally
 500 constrained estimates from ATom-4 flight campaigns, where ~ 30% - 40% DMS was oxidized to
 501 HPMTF along their flight tracks compared to 27.7% for the full branch of HPMTF in the present
 502 work, as well as with previous modeling studies showing 33% HPMTF formation as terminating
 503 product (Veres et al., 2020; Fung et al., 2022). MSA is produced mostly by aqueous phase
 504 oxidation of MSIA by O₃ and OH according to the mechanism used here and has high abundance
 505 near the Southern Ocean and Antarctic belt as reported by previous studies (Chen et al., 2018;
 506 Hoffmann et al., 2016; Fung et al., 2022). The global burden of MSA decreases dramatically, from
 507 19 Gg S for 'Base' to 9.2 Gg S for simulation MOD. The higher rate of major loss process or lower
 508 rate of production of MSA from the aqueous phase reactions could be responsible for this reduction
 509 in global budget (Fung et al., 2022).

510 3.4 Impact on aerosol size distributions

511 Following the percent change in simulated surface layer SO₂ and SO₄²⁻ for modified DMS
 512 chemistry (Fig. 7), we further explore how this expanded DMS oxidation chemistry impacts
 513 modeled aerosol size distributions. Figure 9 shows the global mean surface-layer percent change
 514 in the normalized aerosol number concentration for modified chemistry relative to the BASE

515 simulation, with and without cloud and aerosol HPMTF loss processes. The aerosol number
 516 concentration decreases for the sub-80 nm diameter size bins for both simulations, especially
 517 during the DJF months when cloud and aerosol loss pathways of HPMTF are included (MOD
 518 case), demonstrating the negative impact of these processes on simulated new particle formation.
 519 Without these processes included (as in case MOD_noHetLossHPMTF), percent changes are
 520 lower relative to simulation MOD but similar in terms of direction of changes. On the other hand,
 521 HPMTF lost to clouds and aerosols increases the simulated number of particles with diameter
 522 above 100 nm in the MOD simulation, consistent with the increase in sulfate mass concentrations
 523 shown in Fig. 7 and suggesting that HPMTF heterogenous loss promotes simulated particle growth
 524 to diameters larger than 80-100 nm. The greater abundance of particles larger than 100 nm also
 525 acts as a condensation sink, further suppressing nucleation and growth at smaller size ranges.

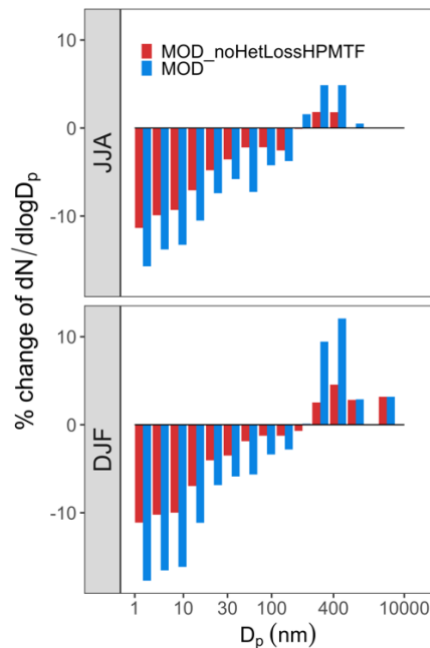


Figure 9 Global mean surface-layer percent change in normalized aerosol number concentration for different size bins with particle diameter, D_p in the range of $3 \text{ nm} < D_p < 10000 \text{ nm}$ for simulations MOD and MOD_noHetLossHPMTF relative to simulation BASE. Simulations are described in Table 5.

526 The geographic distribution of surface layer aerosol number concentration for aerosol in the size
 527 range of 3 – 80 nm for two seasons is shown in Figure 10. We find that global mean aerosol number
 528 concentration in this size range decreases for simulations MOD and MOD_noHetLossHPMTF
 529 relative to BASE by 16.8% and 11.7% respectively. Decreases are greater for simulation MOD
 530 (Fig. 10b). Fig. 10c shows the effect of HPMTF heterogenous loss processes on the number of
 531 particles with diameters between 3-80 nm for simulation MOD relative to simulation
 532 MOD_noHetLossHPMTF. The largely negative impact of HPMTF loss to clouds and aerosols on
 533 sub-80 nm particle number is contributed to by enhanced direct sulfate formation on pre-existing
 534 particles, bypassing gas-phase SO_2 formation (a precursor for new particle formation). As well, in
 535 the model, new particles grow through condensation of H_2SO_4 and organics and their growth are
 536 dependent on the condensation sink, while loss of particle number depends on the coagulation
 537 sink. Thus, changes to the condensation/coagulation sinks and sulfuric acid production rate
 538 through the updated mechanism will also alter the growth rates of small particles (sub-80 nm) as

539 well as their coagulation loss rates. Hence, similar to the discussion for Figure 9, the reduction of
 540 gas-phase production of H_2SO_4 in MOD relative to BASE slows new-particle formation and
 541 growth, while the additional production of sulfate through aqueous chemistry on larger particles
 542 in MOD increases the coagulation scavenging of the newly formed particles. These two effects
 543 synergistically reduce the concentration of ultrafine particles in the model. The fraction of newly
 544 formed particles that can reach the CCN size is dependent on the particle growth rates, especially
 545 for particle sizes below 10 nm, where we see highest coagulation losses to larger particles. The
 546 sensitivity of these results to the new sea salt debromination parameterization is shown in Fig. A4,
 547 where we find a regional increase in aerosol number concentration at mid to higher latitude of the
 548 SH despite low BrO concentrations (Fig A4).

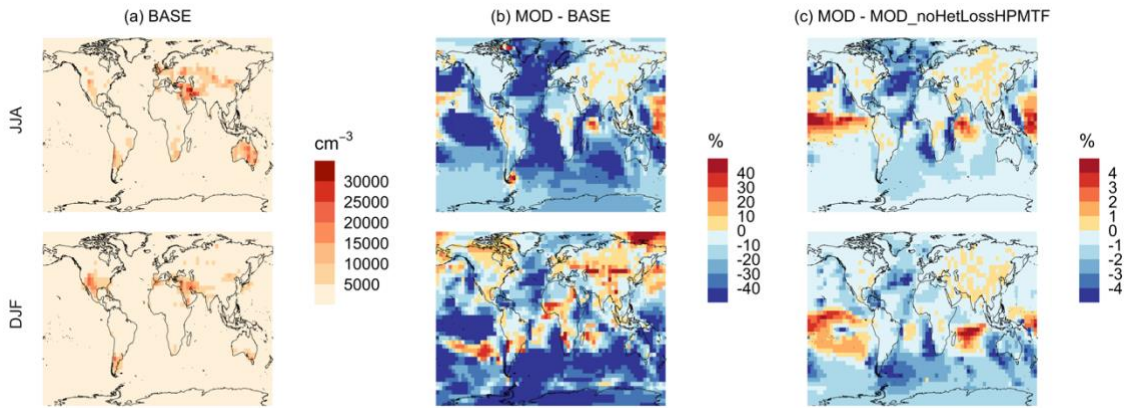


Figure 10 Geographic distribution of seasonal-mean surface-layer aerosol number concentration in cm^{-3} (for particles with diameters between 3 – 80 nm) for (a) the BASE simulation, (b) the percent difference between MOD and BASE and (c) the percent difference between MOD and MOD_noHetLossHPMTF to show the role of cloud and aerosol loss of HPMTF. The top and the bottom rows correspond to the months of JJA and DJF respectively. Simulations are described in Table 5.

549

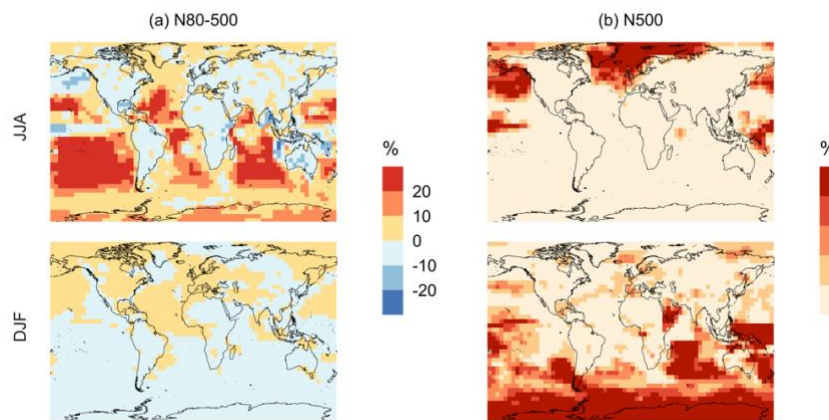


Figure 11 Geographic distribution of percent difference in seasonal-mean surface-layer aerosol number concentration in cm^{-3} for simulations MOD relative to simulations BASE for diameters between (a) 80 – 500 nm and (b) >500 nm. Simulations are described in Table 5.

550 Finally, we also analyze the impact of this expanded DMS scheme on particles larger than 80 nm
 551 (Fig. 11). We find increases of around 6.7% for JJA mean surface layer number concentration of
 552 aerosol with diameters between 80-500 nm, while DJF months show mean reductions of -5.4% for
 553 DJF despite largely positive changes in the marine NH for these months (Fig. 11a). However, for

554 the > 500 nm size ranges (Fig. 11b), the global mean surface layer number concentration of aerosol
555 mostly increases, with highest changes occurring in the areas of peak DMS emission in both
556 hemispheres, during their summertime season. A similar trend is observed in the absence of cloud
557 and aerosol HPMTF uptake in simulation MOD_noHetLossHPMTF (Fig. A5). Overall, the global
558 annual mean number of particles with diameter larger than 80 nm increases by about 3.8%.

559 Comparing the regional extent and direction of change in particle number concentration, we find
560 the net increase in particle number concentration is higher for MOD compared to
561 MOD_noHetLossHPMTF, highlighting the importance of HPMTF loss processes to clouds and
562 aerosols as a contributor of CCN.
563

564 4 Conclusion

565 In this study we update the default DMS oxidation scheme in the GEOS-Chem model by
566 implementing an integrated oxidation mechanism. The new scheme includes gas-phase and
567 aqueous phase reactions involving DMSO, MSIA and HPMTF formation, as well as newly
568 identified HPMTF loss processes yielding considerable changes in seasonal concentrations of
569 major oxidation products and sulfur-derived aerosols. With this new chemistry scheme, global
570 annual mean surface DMS concentration decreases by 36% relative to the BASE scheme in GEOS-
571 Chem globally due to the presence of additional loss processes in the integrated mechanism
572 reducing the bias to ATom-4 DMS measurement.

573 In this new scheme, OH, BrO, O₃ and NO_x species act as important sinks of DMS contributing to
574 66.2%, 18.4%, 3.1% and 11.2% global annual mean surface DMS loss, highlighting the relative
575 importance of these loss process in determining surface DMS budget. We also find that at higher
576 latitudes, gas phase and multiphase oxidation of DMS by O₃ and BrO becomes important to
577 determine the budget of DMS. On the other hand, overall OH is responsible for major loss of DMS
578 via the addition and abstraction reaction relative to other sinks with more contribution from the
579 addition reaction compared to abstraction reaction. For the global distribution of simulated
580 HPMTF, our updated scheme in GEOS-Chem provides a reduced high bias against observations
581 compared to previous studies. While emissions of BrO are uncertain in this version of GEOS-
582 Chem, we find that the compound acts as a key sink of DMS, especially over the Southern Ocean.
583 Overall, we find large reduction in SO₂ (40%) and an increase in sulfate (17%) due to the addition
584 of heterogeneous HPMTF loss processes.

585 The lower SO₂ with the new DMS chemistry scheme contributes to a reduction in the global annual
586 mean surface layer number concentration of particles with diameters less than 80 nm by 16.8%,
587 contributed to by reductions in gas-phase precursors for new particle formation. There is a
588 concurrent increase of 3.8% in the global annual mean number of particles with diameters larger
589 than 80 nm. This latter global mean particle number change varies in sign seasonally, with a 6.7%
590 increase for JJA, and a 5.4% decrease for DJF. This decrease is dominated by southern hemisphere
591 summertime changes, connected with suppressed new particle formation/growth and enhanced
592 coagulation following additional sulfate production through aqueous chemistry. Cloud loss
593 processes related to HPMTF make key contributions to these simulated changes through
594 enhancement of aqueous-phase particle growth of those particle large enough to act as CCN.

595 Although the increased chemical mechanism complexity described in this work will necessarily
596 increase model computational cost (MOD simulation run times increase by approximately 16%),
597 this study highlights the value of including a more realistic chemical oxidation mechanism of DMS
598 and its stable intermediates for better representation of DMS-derived aerosol in the marine
599 atmosphere, as well as its seasonal size distributions. A reduced form of the key chemical species
600 and pathways should be able to capture the key processes with less computational impact and will
601 be a priority in future work.

602 **Appendix A: Additional figures**

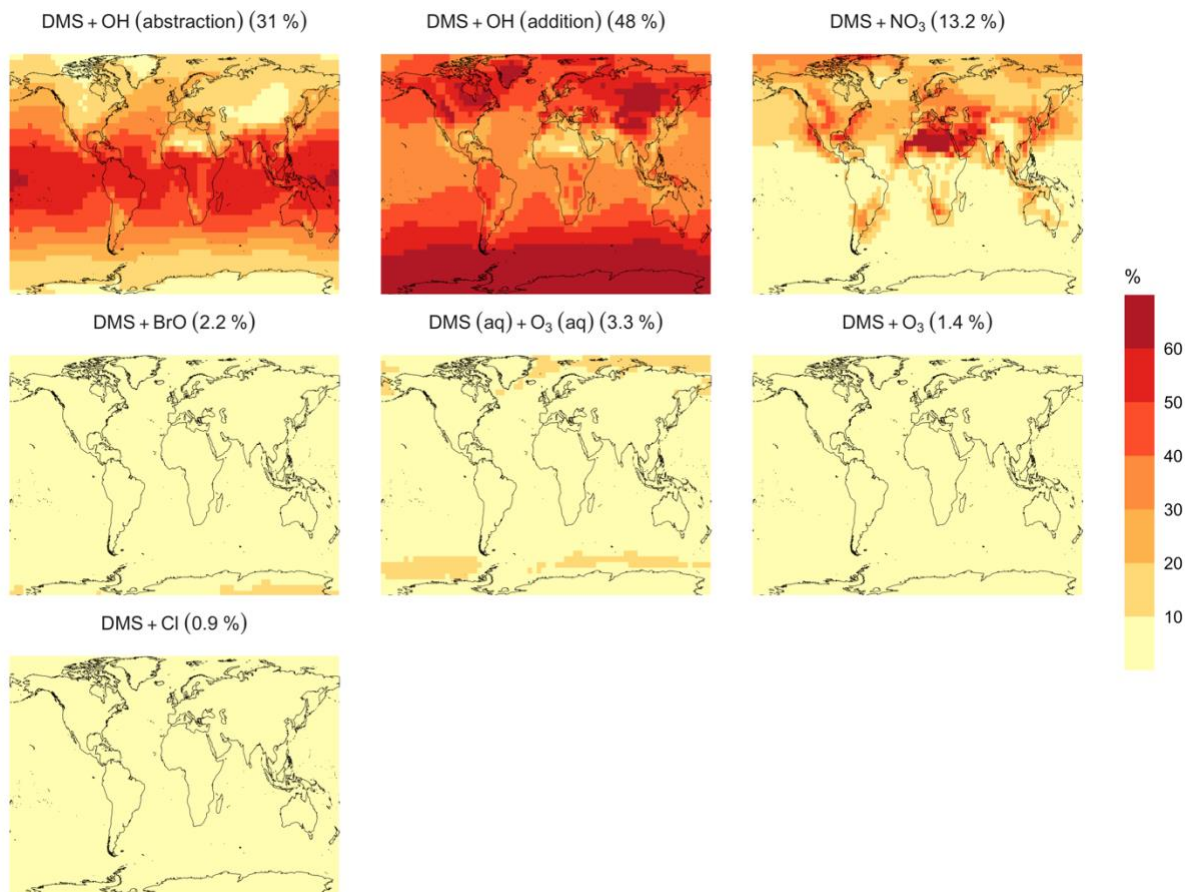


Figure A1 Surface layer geographic distribution of the simulated annual mean fraction of total DMS oxidation (percent) attributed to different tropospheric oxidants for a simulation otherwise the same as simulation MOD except with no sea salt debromination. Percentages in parentheses indicates average contribution to global chemical loss as a fraction of DMS emitted for each reaction pathways presented here. Simulations are described in Table 5.

603

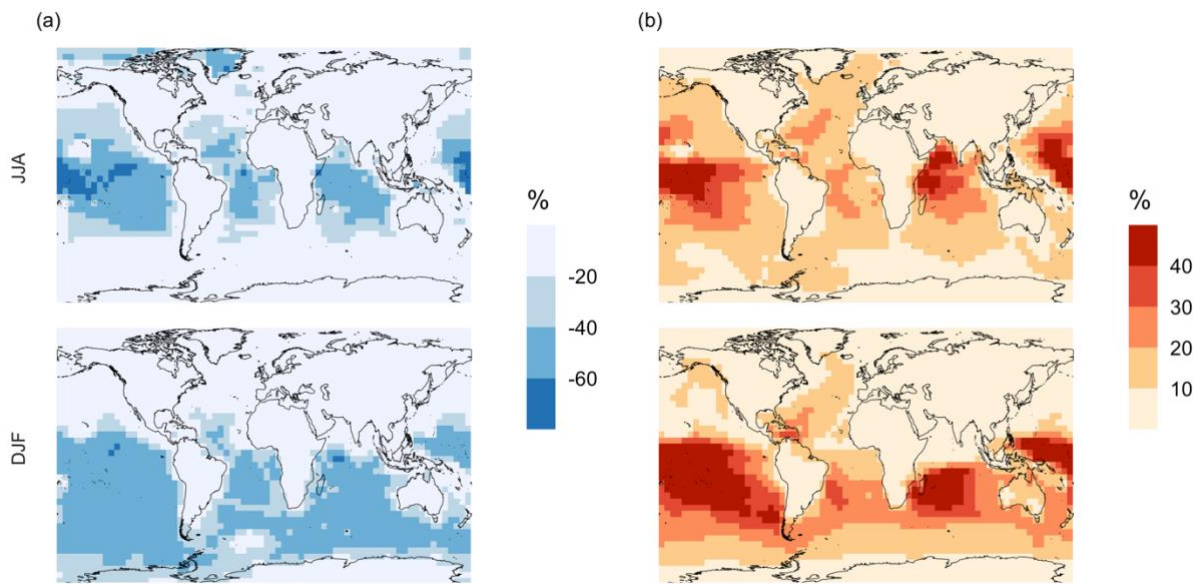


Figure A2 Percent change in simulated surface layer (a) SO_2 and (b) SO_4^{2-} for simulation MOD relative to MOD_noHetLossHPMTF for June, July and August mean (JJA) and December, January, and February mean (DJF). Simulations are described in Table 5.

604

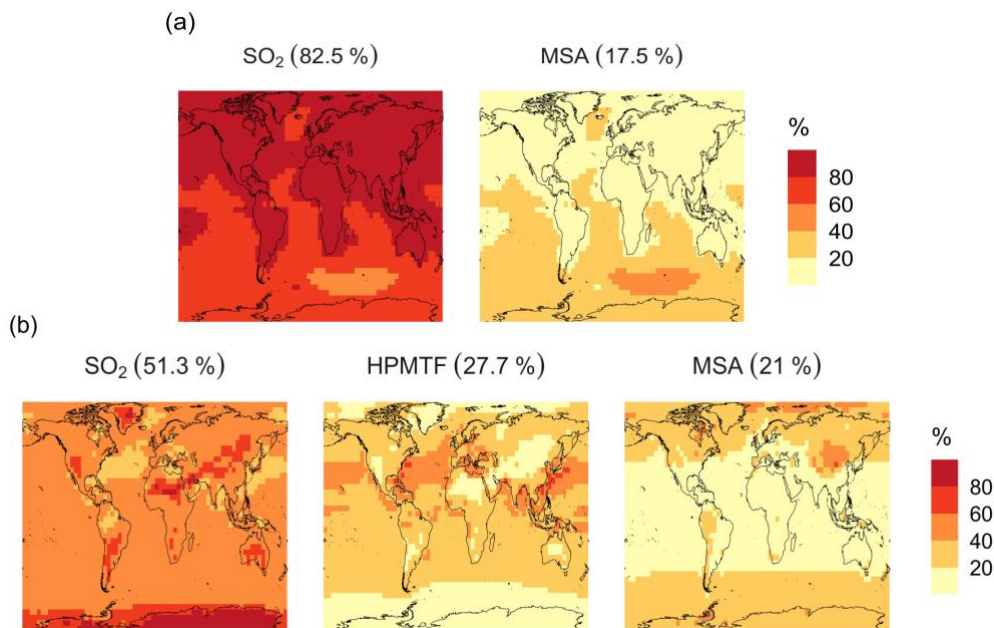


Figure A3 Simulated annual mean surface layer branching ratios (in %) of the DMS oxidation mechanism considering SO_2 , HPMTF, and MSA as major oxidation products calculated from their total production rates for simulations similar to (a, top row) BASE and (b, bottom row) MOD, except MOD with no sea salt debromination. Simulations are described in Table 5.

605

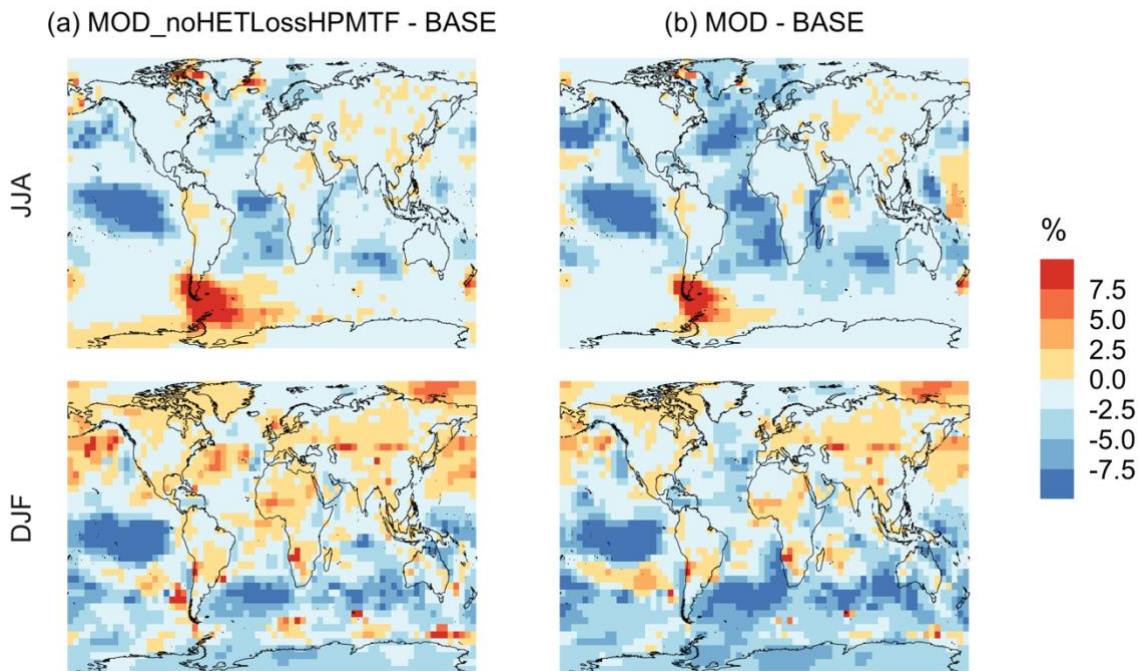


Figure A4 Geographic distribution of percent difference in seasonal-mean surface-layer aerosol number concentration in cm^{-3} (for particles with diameters between 3 – 80 nm) for simulations similar to (a) MOD_noHetLossHPMTF and (b) MOD relative to simulations BASE, except all with no sea salt debromination. Simulations are described in Table 5.

606

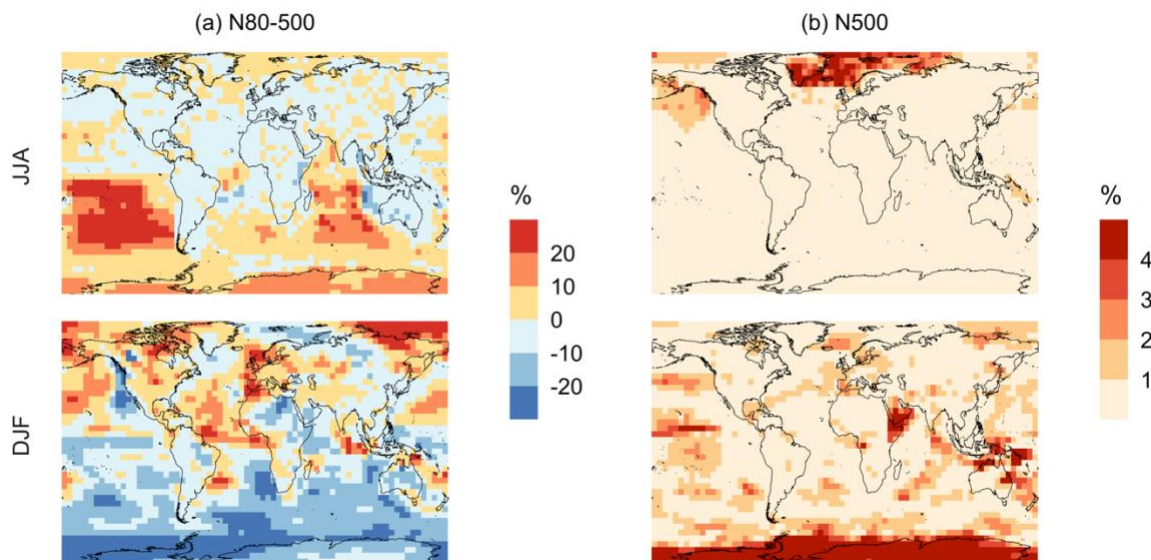


Figure A5 Geographic distribution of percent difference in seasonal-mean surface-layer aerosol number concentration in cm^{-3} for simulations similar to MOD_noHetLossHPMTF relative to simulations BASE, for particle diameters between (a) 80 – 500 nm and (b) > 500 nm. Simulations are described in Table 5.

607

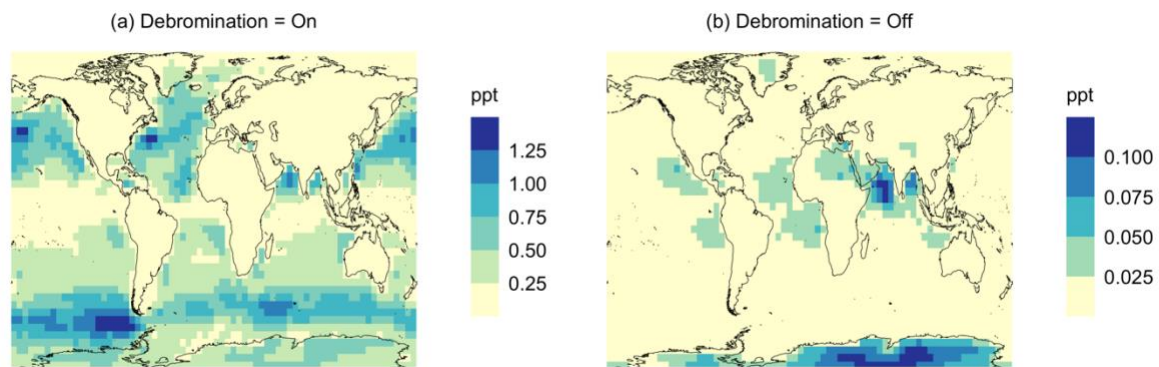


Figure A6 Geographic distribution of mean surface BrO mixing ratio (ppt) for (a) with sea salt debromination and (b) without sea salt debromination for simulation MOD. Simulations are described in Table 5.

608

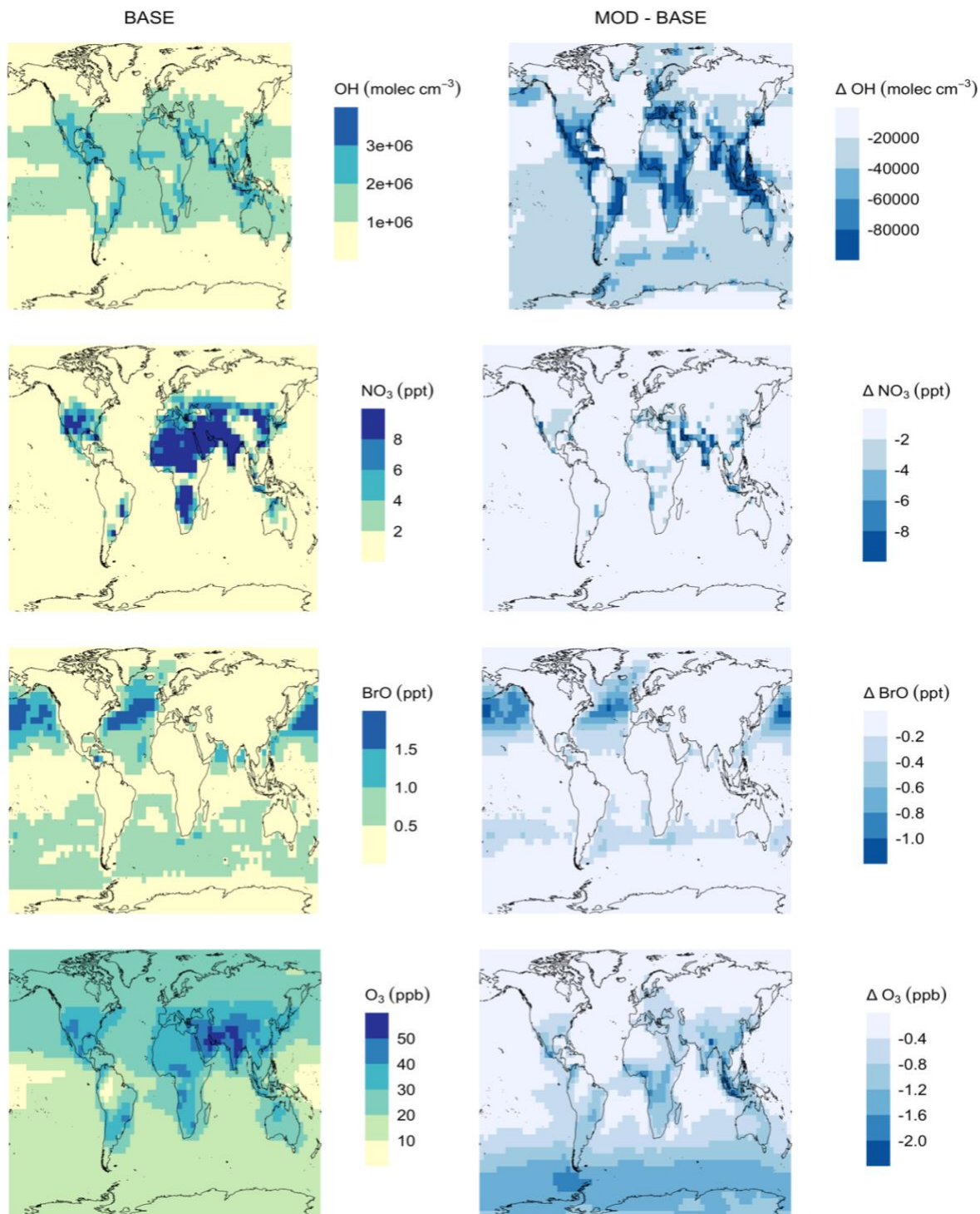


Figure A7 Geographic distribution of mean surface oxidant concentrations for simulation (a) BASE and (b) MOD - BASE. Simulations are described in Table 5.

609

610 **Appendix B: Additional Table**

611 **Table B1.** Global atmospheric flux, deposition, burdens, lifetime of DMS and its oxidation
 612 products, chemical loss rates for specific reaction pathways and global mean concentration of
 613 major oxidants are listed here for the case of simulation MOD. Note that SO₂ and SO₄²⁻ includes
 614 natural as well as anthropogenic sources.

F _{DMS} (Gg S yr ⁻¹)	2.2 × 10 ⁴
Deposition of MSA (Gg S yr ⁻¹)	3.6 × 10 ³
Deposition of HPMTF (Gg S yr ⁻¹)	9.1 × 10 ¹
Deposition of DMSO (Gg S yr ⁻¹)	1.7 × 10 ³
Deposition of MSIA (Gg S yr ⁻¹)	2.1 × 10 ²
DMS (GgS)	65
MSA (GgS)	9.2
HPMTF (GgS)	0.6
SO ₂ (GgS)	256.7
SO ₄ ²⁻ (GgS)	612.4
τ _{DMS} (d)	0.9
τ _{MSA} (d)	0.9
τ _{HPMTF} (d)	0.6
τ _{SO₂} (d)	1.3
τ _{SO₄²⁻} (d)	4.4
DMS lost to MSA (Gg S yr ⁻¹)	4.3 × 10 ³
DMS lost to HPMTF (Gg S yr ⁻¹)	6.9 × 10 ³
DMS lost to SO ₂ (Gg S yr ⁻¹)	9.5 × 10 ³
MSA lost to particle growth (Gg S yr ⁻¹)	4.5 × 10 ²
HPMTF lost to SO ₂ (Gg S yr ⁻¹)	4.8 × 10 ²
HPMTF lost to cloud (Gg S yr ⁻¹)	6.7 × 10 ³
HPMTF lost to particle growth (Gg S yr ⁻¹)	2.8 × 10 ²
OH (molec cm ⁻³)	8.0 × 10 ⁵
NO ₃ (ppt)	0.97
O ₃ (ppb)	21.10
BrO (ppt)	0.31

615
 616 **Data availability.** The DMS observational data in Fig. 2 were obtained from the referenced
 617 papers (Kouvarakis and Mihalopoulos, 2002; Castebrunet et al., 2009). The observations data
 618 during ATom-4 are published through the Distributed Active Archive Center for Biogeochemical
 619 Dynamics (DAAC) at (Novak et al., 2021; Wollesen de Jonge et al., 2021),
 620 <https://doi.org/10.3334/ORNLDAAAC/1921> and
 621 https://daac.ornl.gov/ATOM/guides/ATom_SO2_LIF_Instrument_Data.html.

622 **Author contributions.** LT and WCP designed the research goals, aims, and methodology,
 623 implemented the new code into GC-TOMAS. QC, BA, CHF and CDH contributed in code
 624 development. All authors provided expert advice on data analysis, interpretation, and visualization.
 625 LT ran model simulations, analyzed the data, created the figures, and led manuscript development
 626 and editing.

627 **Competing interests.** The contact authors have declared that none of the authors has any
 628 competing interests.

629 **Acknowledgements.** LT and WCP gratefully acknowledge Ka Ming Fung for discussions on
630 DMS oxidation chemistry. BC thanks Rachel Y.-W. Chang for discussions on marine aerosols.

631 **Financial support.** LT and WCP was supported by NSF grant no. 2155192. QC was supported
632 by the Hong Kong Research Grants Council (Grant No. 15223221 and 15219722). BA was
633 supported by NSF AGS 2109323 and PLR 1904128. CHF was supported by NASA FINESST
634 (grant 80NSSC19K1368). CDH acknowledges funding support from NSF AGS (grant 1848372).
635 BC gratefully acknowledges research funding supported by the Ocean Frontier Institute, through
636 an award from the Canada First Research Excellence Fund. JRP was supported by the Atmospheric
637 System Research (ASR) program, part of the US Department of Energy's Office of Biological and
638 Environmental Research within the Office of Science, under grant DE-SC0021208. SI was
639 supported by Ferring Pharmaceuticals through the Extreme Environments research Laboratory,
640 École Polytechnique Fédérale de Lausanne (EPFL).

641 **References**

642 Adams, P. J. and Seinfeld, J. H.: Predicting global aerosol size distributions in general circulation
643 models, *J. Geophys. Res. Atmospheres*, 107, AAC 4-1-AAC 4-23,
644 <https://doi.org/10.1029/2001JD001010>, 2002.

645 Alexander, B., Park, R. J., Jacob, D. J., Li, Q. B., Yantosca, R. M., Savarino, J., Lee, C. C. W.,
646 and Thiemens, M. H.: Sulfate formation in sea-salt aerosols: Constraints from oxygen isotopes, *J.*
647 *Geophys. Res. Atmospheres*, 110, <https://doi.org/10.1029/2004JD005659>, 2005.

648 Alexander, B., Park, R. J., Jacob, D. J., and Gong, S.: Transition metal-catalyzed oxidation of
649 atmospheric sulfur: Global implications for the sulfur budget, *J. Geophys. Res. Atmospheres*,
650 114, <https://doi.org/10.1029/2008JD010486>, 2009.

651 Amos, H. M., Jacob, D. J., Holmes, C. D., Fisher, J. A., Wang, Q., Yantosca, R. M., Corbitt, E.
652 S., Galarneau, E., Rutter, A. P., Gustin, M. S., Steffen, A., Schauer, J. J., Graydon, J. A., Louis,
653 V. L. S., Talbot, R. W., Edgerton, E. S., Zhang, Y., and Sunderland, E. M.: Gas-particle
654 partitioning of atmospheric Hg(II) and its effect on global mercury deposition, *Atmospheric*
655 *Chem. Phys.*, 12, 591–603, <https://doi.org/10.5194/acp-12-591-2012>, 2012.

656 Atkinson, R., Baulch, D. L., Cox, R. A., Crowley, J. N., Hampson, R. F., Hynes, R. G., Jenkin,
657 M. E., Rossi, M. J., and Troe, J.: Evaluated kinetic and photochemical data for atmospheric
658 chemistry: Volume I - gas phase reactions of O_x, HO_x, NO_x and SO_x species, *Atmospheric*
659 *Chem. Phys.*, 4, 1461–1738, <https://doi.org/10.5194/acp-4-1461-2004>, 2004.

660 Bardouki, H., da Rosa, M. B., Mihalopoulos, N., Palm, W.-U., and Zetzsch, C.: Kinetics and
661 mechanism of the oxidation of dimethylsulfoxide (DMSO) and methanesulfinic acid (MSI⁻) by OH
662 radicals in aqueous medium, *Atmos. Environ.*, 36, 4627–4634, [https://doi.org/10.1016/S1352-](https://doi.org/10.1016/S1352-2310(02)00460-0)
663 [2310\(02\)00460-0](https://doi.org/10.1016/S1352-2310(02)00460-0), 2002.

664 Barnes, I., Hjorth, J., and Mihalopoulos, N.: Dimethyl Sulfide and Dimethyl Sulfoxide and Their
665 Oxidation in the Atmosphere, *Chem. Rev.*, 106, 940–975, <https://doi.org/10.1021/cr020529+>,
666 2006.

667 Barone, S. B., Turnipseed, A. A., and Ravishankara, A. R.: Role of adducts in the atmospheric
668 oxidation of dimethyl sulfide, *Faraday Discuss.*, 100, 39, <https://doi.org/10.1039/fd9950000039>,
669 1995.

670 Berndt, T., Scholz, W., Mentler, B., Fischer, L., Hoffmann, E. H., Tilgner, A., Hyttinen, N.,
671 Prisle, N. L., Hansel, A., and Herrmann, H.: Fast Peroxy Radical Isomerization and OH
672 Recycling in the Reaction of OH Radicals with Dimethyl Sulfide, *J. Phys. Chem. Lett.*, 10,
673 6478–6483, <https://doi.org/10.1021/acs.jpcclett.9b02567>, 2019.

674 Berndt, T., Hoffmann, E. H., Tilgner, A., Stratmann, F., and Herrmann, H.: Direct sulfuric acid
675 formation from the gas-phase oxidation of reduced-sulfur compounds, *Nat. Commun.*, 14, 4849,
676 <https://doi.org/10.1038/s41467-023-40586-2>, 2023.

677 Bey, I., Jacob, D. J., Yantosca, R. M., Logan, J. A., Field, B. D., Fiore, A. M., Li, Q., Liu, H. Y.,
678 Mickley, L. J., and Schultz, M. G.: Global modeling of tropospheric chemistry with assimilated
679 meteorology: Model description and evaluation, *J. Geophys. Res. Atmospheres*, 106, 23073–
680 23095, <https://doi.org/10.1029/2001JD000807>, 2001.

681 Boniface, J., Shi, Q., Li, Y. Q., Cheung, J. L., Rattigan, O. V., Davidovits, P., Worsnop, D. R.,
682 Jayne, J. T., and Kolb, C. E.: Uptake of Gas-Phase SO₂, H₂S, and CO₂ by Aqueous Solutions, *J.*
683 *Phys. Chem. A*, 104, 7502–7510, <https://doi.org/10.1021/jp000479h>, 2000.

684 Borissenko, D., Kukui, A., Laverdet, G., and Le Bras, G.: Experimental Study of SO₂ Formation
685 in the Reactions of CH₃SO Radical with NO₂ and O₃ in Relation with the Atmospheric
686 Oxidation Mechanism of Dimethyl Sulfide, *J. Phys. Chem. A*, 107, 1155–1161,
687 <https://doi.org/10.1021/jp021701g>, 2003.

688 Boucher, O., Moulin, C., Belviso, S., Aumont, O., Bopp, L., Cosme, E., von Kuhlmann, R.,
689 Lawrence, M. G., Pham, M., Reddy, M. S., Sciare, J., and Venkataraman, C.: DMS atmospheric
690 concentrations and sulphate aerosol indirect radiative forcing: a sensitivity study to the DMS
691 source representation and oxidation, *Atmospheric Chem. Phys.*, 3, 49–65,
692 <https://doi.org/10.5194/acp-3-49-2003>, 2003.

693 Bräuer, P., Tilgner, A., Wolke, R., and Herrmann, H.: Mechanism development and modelling of
694 tropospheric multiphase halogen chemistry: The CAPRAM Halogen Module 2.0 (HM2), *J.*
695 *Atmospheric Chem.*, 70, 19–52, <https://doi.org/10.1007/s10874-013-9249-6>, 2013.

696 Breider, T. J., Chipperfield, M. P., Richards, N. a. D., Carslaw, K. S., Mann, G. W., and
697 Spracklen, D. V.: Impact of BrO on dimethylsulfide in the remote marine boundary layer,
698 *Geophys. Res. Lett.*, 37, <https://doi.org/10.1029/2009GL040868>, 2010.

699 Burkholder, J. B., Sander, S. P., Abbatt, J. P. D., Barker, J. R., Cappa, C., Crouse, J. D., Dibble,
700 T. S., Huie, R. E., Kolb, C. E., Kurylo, M. J., Orkin, V. L., Percival, C. J., Wilmouth, D. M., and
701 Wine, P. H.: Chemical kinetics and photochemical data for use in atmospheric studies;
702 evaluation number 19, 2020.

703 Cala, B. A., Archer-Nicholls, S., Weber, J., Abraham, N. L., Griffiths, P. T., Jacob, L., Shin, Y.
704 M., Revell, L. E., Woodhouse, M., and Archibald, A. T.: Development, intercomparison, and

705 evaluation of an improved mechanism for the oxidation of dimethyl sulfide in the UKCA model,
706 *Atmospheric Chem. Phys.*, 23, 14735–14760, <https://doi.org/10.5194/acp-23-14735-2023>, 2023.

707 Campolongo, F., Saltelli, A., Jensen, N. R., Wilson, J., and Hjorth, J.: The Role of Multiphase
708 Chemistry in the Oxidation of Dimethylsulphide (DMS). A Latitude Dependent Analysis, *J.*
709 *Atmospheric Chem.*, 32, 327–356, <https://doi.org/10.1023/A:1006154618511>, 1999.

710 Carslaw, K. S., Lee, L. A., Reddington, C. L., Pringle, K. J., Rap, A., Forster, P. M., Mann, G.
711 W., Spracklen, D. V., Woodhouse, M. T., Regayre, L. A., and Pierce, J. R.: Large contribution of
712 natural aerosols to uncertainty in indirect forcing, *Nature*, 503, 67–71,
713 <https://doi.org/10.1038/nature12674>, 2013.

714 Castebrunet, H., Martinerie, P., Genthon, C., and Cosme, E.: A three-dimensional model study of
715 methanesulphonic acid to non sea salt sulphate ratio at mid and high-southern latitudes,
716 *Atmospheric Chem. Phys.*, 9, 9449–9469, <https://doi.org/10.5194/acp-9-9449-2009>, 2009.

717 Charlson, R. J., Lovelock, J. E., Andreae, M. O., and Warren, S. G.: Oceanic phytoplankton,
718 atmospheric sulphur, cloud albedo and climate, *Nature*, 326, 655–661,
719 <https://doi.org/10.1038/326655a0>, 1987.

720 Chen, H., Ezell, M. J., Arquero, K. D., Varner, M. E., Dawson, M. L., Gerber, R. B., and
721 Finlayson-Pitts, B. J.: New particle formation and growth from methanesulfonic acid,
722 trimethylamine and water, *Phys. Chem. Chem. Phys.*, 17, 13699–13709,
723 <https://doi.org/10.1039/C5CP00838G>, 2015.

724 Chen, Q., Geng, L., Schmidt, J. A., Xie, Z., Kang, H., Dachs, J., Cole-Dai, J., Schauer, A. J.,
725 Camp, M. G., and Alexander, B.: Isotopic constraints on the role of hypohalous acids in sulfate
726 aerosol formation in the remote marine boundary layer, *Atmospheric Chem. Phys.*, 16, 11433–
727 11450, <https://doi.org/10.5194/acp-16-11433-2016>, 2016.

728 Chen, Q., Schmidt, J. A., Shah, V., Jaeglé, L., Sherwen, T., and Alexander, B.: Sulfate
729 production by reactive bromine: Implications for the global sulfur and reactive bromine budgets,
730 *Geophys. Res. Lett.*, 44, 7069–7078, <https://doi.org/10.1002/2017GL073812>, 2017.

731 Chen, Q., Sherwen, T., Evans, M., and Alexander, B.: DMS oxidation and sulfur aerosol
732 formation in the marine troposphere: a focus on reactive halogen and multiphase chemistry,
733 *Atmospheric Chem. Phys.*, 18, 13617–13637, <https://doi.org/10.5194/acp-18-13617-2018>, 2018.

734 Chin, M., Jacob, D. J., Gardner, G. M., Foreman-Fowler, M. S., Spiro, P. A., and Savoie, D. L.:
735 A global three-dimensional model of tropospheric sulfate, *J. Geophys. Res. Atmospheres*, 101,
736 18667–18690, <https://doi.org/10.1029/96JD01221>, 1996.

737 Clarke, A. D., Davis, D., Kapustin, V. N., Eisele, F., Chen, G., Paluch, I., Lenschow, D., Bandy,
738 A. R., Thornton, D., Moore, K., Mauldin, L., Tanner, D., Litchy, M., Carroll, M. A., Collins, J.,
739 and Albercook, G.: Particle Nucleation in the Tropical Boundary Layer and Its Coupling to
740 Marine Sulfur Sources, *Science*, 282, 89–92, 1998a.

741 Clarke, A. D., Varner, J. L., Eisele, F., Mauldin, R. L., Tanner, D., and Litchy, M.: Particle
742 production in the remote marine atmosphere: Cloud outflow and subsidence during ACE 1, *J.*
743 *Geophys. Res. Atmospheres*, 103, 16397–16409, <https://doi.org/10.1029/97JD02987>, 1998b.

744 Du, L., Xu, Y., Ge, M., Jia, L., Yao, L., and Wang, W.: Rate constant of the gas phase reaction
745 of dimethyl sulfide (CH₃SCH₃) with ozone, *Chem. Phys. Lett.*, 436, 36–40,
746 <https://doi.org/10.1016/j.cplett.2007.01.025>, 2007.

747 Duncan Fairlie, T., Jacob, D. J., and Park, R. J.: The impact of transpacific transport of mineral
748 dust in the United States, *Atmos. Environ.*, 41, 1251–1266,
749 <https://doi.org/10.1016/j.atmosenv.2006.09.048>, 2007.

750 Emerson, E. W., Hodshire, A. L., DeBolt, H. M., Billsback, K. R., Pierce, J. R., McMeeking, G.
751 R., and Farmer, D. K.: Revisiting particle dry deposition and its role in radiative effect estimates,
752 *Proc. Natl. Acad. Sci.*, 117, 26076–26082, <https://doi.org/10.1073/pnas.2014761117>, 2020.

753 Enami, S., Nakano, Y., Hashimoto, S., Kawasaki, M., Aloisio, S., and Francisco, J. S.: Reactions
754 of Cl Atoms with Dimethyl Sulfide: A Theoretical Calculation and an Experimental Study with
755 Cavity Ring-Down Spectroscopy, *J. Phys. Chem. A*, 108, 7785–7789,
756 <https://doi.org/10.1021/jp049772y>, 2004.

757 Faloon, I.: Sulfur processing in the marine atmospheric boundary layer: A review and critical
758 assessment of modeling uncertainties, *Atmos. Environ.*, 43, 2841–2854,
759 <https://doi.org/10.1016/j.atmosenv.2009.02.043>, 2009.

760 Flyunt, R., Makogon, O., Schuchmann, M. N., Asmus, K.-D., and Sonntag, C. von: OH-Radical-
761 induced oxidation of methanesulfinic acid. The reactions of the methanesulfonyl radical in the
762 absence and presence of dioxygen, *J. Chem. Soc. Perkin Trans. 2*, 787–792,
763 <https://doi.org/10.1039/B009631H>, 2001.

764 Fung, K. M., Heald, C. L., Kroll, J. H., Wang, S., Jo, D. S., Gettelman, A., Lu, Z., Liu, X.,
765 Zaveri, R. A., Apel, E. C., Blake, D. R., Jimenez, J.-L., Campuzano-Jost, P., Veres, P. R., Bates,
766 T. S., Shilling, J. E., and Zawadowicz, M.: Exploring dimethyl sulfide (DMS) oxidation and
767 implications for global aerosol radiative forcing, *Atmospheric Chem. Phys.*, 22, 1549–1573,
768 <https://doi.org/10.5194/acp-22-1549-2022>, 2022.

769 Galí, M., Lévassieur, M., Devred, E., Simó, R., and Babin, M.: Sea-surface dimethylsulfide
770 (DMS) concentration from satellite data at global and regional scales, *Biogeosciences*, 15, 3497–
771 3519, <https://doi.org/10.5194/bg-15-3497-2018>, 2018.

772 Galí, M., Devred, E., Babin, M., and Lévassieur, M.: Decadal increase in Arctic dimethylsulfide
773 emission, *Proc. Natl. Acad. Sci.*, 116, 19311–19317, <https://doi.org/10.1073/pnas.1904378116>,
774 2019.

775 Gershenson, M., Davidovits, P., Jayne, J. T., Kolb, C. E., and Worsnop, D. R.: Simultaneous
776 Uptake of DMS and Ozone on Water, *J. Phys. Chem. A*, 105, 7031–7036,
777 <https://doi.org/10.1021/jp010696y>, 2001.

778 von Glasow, R. and Crutzen, P. J.: Model study of multiphase DMS oxidation with a focus on
779 halogens, *Atmospheric Chem. Phys.*, 4, 589–608, <https://doi.org/10.5194/acp-4-589-2004>, 2004.

780 Herrmann, H., Zellner, R., Mirabel, P., Buxton, G., Salmon, A., Sehested, K., Holcman, J., and
781 Brede, O.: Removal and interconversions of oxidants in the atmospheric aqueous phase, part 2
782 (RINOXA 2). Final report, Universität GH Essen. Institut für Physikalische und Theoretische
783 Chemie, Essen, 1998.

784 Hezel, P. J., Alexander, B., Bitz, C. M., Steig, E. J., Holmes, C. D., Yang, X., and Sciare, J.:
785 Modeled methanesulfonic acid (MSA) deposition in Antarctica and its relationship to sea ice, *J.*
786 *Geophys. Res. Atmospheres*, 116, <https://doi.org/10.1029/2011JD016383>, 2011.

787 Hodshire, A. L., Campuzano-Jost, P., Kodros, J. K., Croft, B., Nault, B. A., Schroder, J. C.,
788 Jimenez, J. L., and Pierce, J. R.: The potential role of methanesulfonic acid (MSA) in aerosol
789 formation and growth and the associated radiative forcings, *Atmospheric Chem. Phys.*, 19,
790 3137–3160, <https://doi.org/10.5194/acp-19-3137-2019>, 2019.

791 Hoffmann, E. H., Tilgner, A., Schrödner, R., Bräuer, P., Wolke, R., and Herrmann, H.: An
792 advanced modeling study on the impacts and atmospheric implications of multiphase dimethyl
793 sulfide chemistry, *Proc. Natl. Acad. Sci.*, 113, 11776–11781,
794 <https://doi.org/10.1073/pnas.1606320113>, 2016.

795 Hoffmann, E. H., Heinold, B., Kubin, A., Tegen, I., and Herrmann, H.: The Importance of the
796 Representation of DMS Oxidation in Global Chemistry-Climate Simulations, *Geophys. Res.*
797 *Lett.*, 48, e2021GL094068, <https://doi.org/10.1029/2021GL094068>, 2021.

798 Holmes, C. D., Bertram, T. H., Confer, K. L., Graham, K. A., Ronan, A. C., Wirks, C. K., and
799 Shah, V.: The Role of Clouds in the Tropospheric NO_x Cycle: A New Modeling Approach for
800 Cloud Chemistry and Its Global Implications, *Geophys. Res. Lett.*, 46, 4980–4990,
801 <https://doi.org/10.1029/2019GL081990>, 2019.

802 Hoyle, C. R., Fuchs, C., Järvinen, E., Saathoff, H., Dias, A., El Haddad, I., Gysel, M., Coburn, S.
803 C., Tröstl, J., Bernhammer, A.-K., Bianchi, F., Breitenlechner, M., Corbin, J. C., Craven, J.,
804 Donahue, N. M., Duplissy, J., Ehrhart, S., Frege, C., Gordon, H., Höppel, N., Heinritzi, M.,
805 Kristensen, T. B., Molteni, U., Nichman, L., Pinterich, T., Prévôt, A. S. H., Simon, M., Slowik,
806 J. G., Steiner, G., Tomé, A., Vogel, A. L., Volkamer, R., Wagner, A. C., Wagner, R., Wexler, A.
807 S., Williamson, C., Winkler, P. M., Yan, C., Amorim, A., Dommen, J., Curtius, J., Gallagher, M.
808 W., Flagan, R. C., Hansel, A., Kirkby, J., Kulmala, M., Möhler, O., Stratmann, F., Worsnop, D.
809 R., and Baltensperger, U.: Aqueous phase oxidation of sulphur dioxide by ozone in cloud
810 droplets, *Atmospheric Chem. Phys.*, 16, 1693–1712, <https://doi.org/10.5194/acp-16-1693-2016>,
811 2016.

812 Ishino, S., Hattori, S., Legrand, M., Chen, Q., Alexander, B., Shao, J., Huang, J., Jaeglé, L.,
813 Jourdain, B., Preunkert, S., Yamada, A., Yoshida, N., and Savarino, J.: Regional Characteristics
814 of Atmospheric Sulfate Formation in East Antarctica Imprinted on 17O-Excess Signature, *J.*
815 *Geophys. Res. Atmospheres*, 126, e2020JD033583, <https://doi.org/10.1029/2020JD033583>,
816 2021.

817 Jacob, D. J., Field, B. D., Li, Q., Blake, D. R., de Gouw, J., Warneke, C., Hansel, A., Wisthaler,
818 A., Singh, H. B., and Guenther, A.: Global budget of methanol: Constraints from atmospheric
819 observations, *J. Geophys. Res. Atmospheres*, 110, <https://doi.org/10.1029/2004JD005172>, 2005.

820 Jernigan, C. M., Fite, C. H., Vereecken, L., Berkelhammer, M. B., Rollins, A. W., Rickly, P. S.,
821 Novelli, A., Taraborrelli, D., Holmes, C. D., and Bertram, T. H.: Efficient Production of
822 Carbonyl Sulfide in the Low-NO_x Oxidation of Dimethyl Sulfide, *Geophys. Res. Lett.*, 49,
823 e2021GL096838, <https://doi.org/10.1029/2021GL096838>, 2022a.

824 Jernigan, C. M., Cappa, C. D., and Bertram, T. H.: Reactive Uptake of Hydroperoxymethyl
825 Thioformate to Sodium Chloride and Sodium Iodide Aerosol Particles, *J. Phys. Chem. A*, 126,
826 4476–4481, <https://doi.org/10.1021/acs.jpca.2c03222>, 2022b.

827 Johnson, J. S. and Jen, C. N.: Role of Methanesulfonic Acid in Sulfuric Acid–Amine and
828 Ammonia New Particle Formation, *ACS Earth Space Chem.*, 7, 653–660,
829 <https://doi.org/10.1021/acsearthspacechem.3c00017>, 2023.

830 Johnson, M. T.: A numerical scheme to calculate temperature and salinity dependent air-water
831 transfer velocities for any gas, *Ocean Sci.*, 6, 913–932, <https://doi.org/10.5194/os-6-913-2010>,
832 2010.

833 Kaufman, Y. J. and Tanré, D.: Effect of variations in super-saturation on the formation of cloud
834 condensation nuclei, *Nature*, 369, 45–48, <https://doi.org/10.1038/369045a0>, 1994.

835 Khan, M. A. H., Gillespie, S. M. P., Razis, B., Xiao, P., Davies-Coleman, M. T., Percival, C. J.,
836 Derwent, R. G., Dyke, J. M., Ghosh, M. V., Lee, E. P. F., and Shallcross, D. E.: A modelling
837 study of the atmospheric chemistry of DMS using the global model, STOCHEM-CRI, *Atmos.*
838 *Environ.*, 127, 69–79, <https://doi.org/10.1016/j.atmosenv.2015.12.028>, 2016.

839 Khan, M. A. H., Bannan, T. J., Holland, R., Shallcross, D. E., Archibald, A. T., Matthews, E.,
840 Back, A., Allan, J., Coe, H., Artaxo, P., and Percival, C. J.: Impacts of Hydroperoxymethyl
841 Thioformate on the Global Marine Sulfur Budget, *ACS Earth Space Chem.*, 5, 2577–2586,
842 <https://doi.org/10.1021/acsearthspacechem.1c00218>, 2021.

843 Kloster, S., Feichter, J., Maier-Reimer, E., Six, K. D., Stier, P., and Wetzol, P.: DMS cycle in the
844 marine ocean-atmosphere system – a global model study, *Biogeosciences*, 3, 29–51,
845 <https://doi.org/10.5194/bg-3-29-2006>, 2006.

846 Kodros, J. K. and Pierce, J. R.: Important global and regional differences in aerosol cloud-albedo
847 effect estimates between simulations with and without prognostic aerosol microphysics, *J.*
848 *Geophys. Res. Atmospheres*, 122, 4003–4018, <https://doi.org/10.1002/2016JD025886>, 2017.

849 Kodros, J. K., Cucinotta, R., Ridley, D. A., Wiedinmyer, C., and Pierce, J. R.: The aerosol
850 radiative effects of uncontrolled combustion of domestic waste, *Atmospheric Chem. Phys.*, 16,
851 6771–6784, <https://doi.org/10.5194/acp-16-6771-2016>, 2016.

852 Kouvarakis, G. and Mihalopoulos, N.: Seasonal variation of dimethylsulfide in the gas phase and
853 of methanesulfonate and non-sea-salt sulfate in the aerosols phase in the Eastern Mediterranean

854 atmosphere, *Atmos. Environ.*, 36, 929–938, [https://doi.org/10.1016/S1352-2310\(01\)00511-8](https://doi.org/10.1016/S1352-2310(01)00511-8),
855 2002.

856 Kowalczyk, P., Cooper, W. J., Whitehead, R. F., Durako, M. J., and Sheldon, W.:
857 Characterization of CDOM in an organic-rich river and surrounding coastal ocean in the South
858 Atlantic Bight, *Aquat. Sci.*, 65, 384–401, <https://doi.org/10.1007/s00027-003-0678-1>, 2003.

859 Kulmala, M.: How Particles Nucleate and Grow, *Science*, 302, 1000–1001,
860 <https://doi.org/10.1126/science.1090848>, 2003.

861 Kulmala, M., Pirjola, L., and Mäkelä, J. M.: Stable sulphate clusters as a source of new
862 atmospheric particles, *Nature*, 404, 66–69, <https://doi.org/10.1038/35003550>, 2000.

863 Lana, A., Bell, T. G., Simó, R., Vallina, S. M., Ballabrera-Poy, J., Kettle, A. J., Dachs, J., Bopp,
864 L., Saltzman, E. S., Stefels, J., Johnson, J. E., and Liss, P. S.: An updated climatology of surface
865 dimethylsulfide concentrations and emission fluxes in the global ocean, *Glob. Biogeochem.*
866 *Cycles*, 25, <https://doi.org/10.1029/2010GB003850>, 2011.

867 Leaitch, W. R., Sharma, S., Huang, L., Toom-Sauntry, D., Chivulescu, A., Macdonald, A. M.,
868 von Salzen, K., Pierce, J. R., Bertram, A. K., Schroder, J. C., Shantz, N. C., Chang, R. Y.-W.,
869 and Norman, A.-L.: Dimethyl sulfide control of the clean summertime Arctic aerosol and cloud,
870 *Elem. Sci. Anthr.*, 1, 000017, <https://doi.org/10.12952/journal.elementa.000017>, 2013.

871 Lee, Y. H. and Adams, P. J.: A Fast and Efficient Version of the Two-Moment Aerosol
872 Sectional (TOMAS) Global Aerosol Microphysics Model, *Aerosol Sci. Technol.*, 46, 678–689,
873 <https://doi.org/10.1080/02786826.2011.643259>, 2012.

874 Lee, Y. H., Pierce, J. R., and Adams, P. J.: Representation of nucleation mode microphysics in a
875 global aerosol model with sectional microphysics, *Geosci. Model Dev.*, 6, 1221–1232,
876 <https://doi.org/10.5194/gmd-6-1221-2013>, 2013.

877 Lennartz, S. T., Krysztofiak, G., Marandino, C. A., Sinnhuber, B.-M., Tegtmeier, S., Ziska, F.,
878 Hossaini, R., Krüger, K., Montzka, S. A., Atlas, E., Oram, D. E., Keber, T., Bönisch, H., and
879 Quack, B.: Modelling marine emissions and atmospheric distributions of halocarbons and
880 dimethyl sulfide: the influence of prescribed water concentration vs. prescribed emissions,
881 *Atmospheric Chem. Phys.*, 15, 11753–11772, <https://doi.org/10.5194/acp-15-11753-2015>, 2015.

882 Liu, H., Jacob, D. J., Bey, I., and Yantosca, R. M.: Constraints from ²¹⁰Pb and ⁷Be on wet
883 deposition and transport in a global three-dimensional chemical tracer model driven by
884 assimilated meteorological fields, *J. Geophys. Res. Atmospheres*, 106, 12109–12128,
885 <https://doi.org/10.1029/2000JD900839>, 2001.

886 Lucas, D. D. and Prinn, R. G.: Mechanistic studies of dimethylsulfide oxidation products using
887 an observationally constrained model, *J. Geophys. Res. Atmospheres*, 107, ACH 12-1-ACH 12-
888 26, <https://doi.org/10.1029/2001JD000843>, 2002.

- 889 Napari, I., Noppel, M., Vehkamäki, H., and Kulmala, M.: Parametrization of ternary nucleation
890 rates for H₂SO₄-NH₃-H₂O vapors, *J. Geophys. Res. Atmospheres*, 107, AAC 6-1-AAC 6-6,
891 <https://doi.org/10.1029/2002JD002132>, 2002.
- 892 Nightingale, P. D., Malin, G., Law, C. S., Watson, A. J., Liss, P. S., Liddicoat, M. I., Boutin, J.,
893 and Upstill-Goddard, R. C.: In situ evaluation of air-sea gas exchange parameterizations using
894 novel conservative and volatile tracers, *Glob. Biogeochem. Cycles*, 14, 373–387,
895 <https://doi.org/10.1029/1999GB900091>, 2000.
- 896 Novak, G. A., Fite, C. H., Holmes, C. D., Veres, P. R., Neuman, J. A., Faloona, I., Thornton, J.
897 A., Wolfe, G. M., Vermeuel, M. P., Jernigan, C. M., Peischl, J., Ryerson, T. B., Thompson, C.
898 R., Bourgeois, I., Warneke, C., Gkatzelis, G. I., Coggon, M. M., Sekimoto, K., Bui, T. P., Dean-
899 Day, J., Diskin, G. S., DiGangi, J. P., Nowak, J. B., Moore, R. H., Wiggins, E. B., Winstead, E.
900 L., Robinson, C., Thornhill, K. L., Sanchez, K. J., Hall, S. R., Ullmann, K., Dollner, M.,
901 Weinzierl, B., Blake, D. R., and Bertram, T. H.: Rapid cloud removal of dimethyl sulfide
902 oxidation products limits SO₂ and cloud condensation nuclei production in the marine
903 atmosphere, *Proc. Natl. Acad. Sci.*, 118, e2110472118,
904 <https://doi.org/10.1073/pnas.2110472118>, 2021.
- 905 Novak, G. A., Kilgour, D. B., Jernigan, C. M., Vermeuel, M. P., and Bertram, T. H.: Oceanic
906 emissions of dimethyl sulfide and methanethiol and their contribution to sulfur dioxide
907 production in the marine atmosphere, *Atmospheric Chem. Phys.*, 22, 6309–6325,
908 <https://doi.org/10.5194/acp-22-6309-2022>, 2022.
- 909 Park, R. J., Jacob, D. J., Field, B. D., Yantosca, R. M., and Chin, M.: Natural and transboundary
910 pollution influences on sulfate-nitrate-ammonium aerosols in the United States: Implications for
911 policy, *J. Geophys. Res. Atmospheres*, 109, <https://doi.org/10.1029/2003JD004473>, 2004.
- 912 Parrella, J. P., Jacob, D. J., Liang, Q., Zhang, Y., Mickley, L. J., Miller, B., Evans, M. J., Yang,
913 X., Pyle, J. A., Theys, N., and Van Roozendaal, M.: Tropospheric bromine chemistry:
914 implications for present and pre-industrial ozone and mercury, *Atmospheric Chem. Phys.*, 12,
915 6723–6740, <https://doi.org/10.5194/acp-12-6723-2012>, 2012.
- 916 Pierce, J. R. and Adams, P. J.: Global evaluation of CCN formation by direct emission of sea salt
917 and growth of ultrafine sea salt, *J. Geophys. Res. Atmospheres*, 111,
918 <https://doi.org/10.1029/2005JD006186>, 2006.
- 919 Pound, R. J., Sherwen, T., Helmig, D., Carpenter, L. J., and Evans, M. J.: Influences of oceanic
920 ozone deposition on tropospheric photochemistry, *Atmospheric Chem. Phys.*, 20, 4227–4239,
921 <https://doi.org/10.5194/acp-20-4227-2020>, 2020.
- 922 Pye, H. O. T., Liao, H., Wu, S., Mickley, L. J., Jacob, D. J., Henze, D. K., and Seinfeld, J. H.:
923 Effect of changes in climate and emissions on future sulfate-nitrate-ammonium aerosol levels in
924 the United States, *J. Geophys. Res. Atmospheres*, 114, <https://doi.org/10.1029/2008JD010701>,
925 2009.
- 926 Rosati, B., Isokääntä, S., Christiansen, S., Jensen, M. M., Moosakutty, S. P., Wollesen de Jonge,
927 R., Massling, A., Glasius, M., Elm, J., Virtanen, A., and Bilde, M.: Hygroscopicity and CCN

- 928 potential of DMS-derived aerosol particles, *Atmospheric Chem. Phys.*, 22, 13449–13466,
929 <https://doi.org/10.5194/acp-22-13449-2022>, 2022.
- 930 Schmidt, J. A., Jacob, D. J., Horowitz, H. M., Hu, L., Sherwen, T., Evans, M. J., Liang, Q.,
931 Suleiman, R. M., Oram, D. E., Le Breton, M., Percival, C. J., Wang, S., Dix, B., and Volkamer,
932 R.: Modeling the observed tropospheric BrO background: Importance of multiphase chemistry
933 and implications for ozone, OH, and mercury, *J. Geophys. Res. Atmospheres*, 121, 11,819-
934 11,835, <https://doi.org/10.1002/2015JD024229>, 2016.
- 935 Schobesberger, S., Junninen, H., Bianchi, F., Lönn, G., Ehn, M., Lehtipalo, K., Dommen, J.,
936 Ehrhart, S., Ortega, I. K., Franchin, A., Nieminen, T., Riccobono, F., Hutterli, M., Duplissy, J.,
937 Almeida, J., Amorim, A., Breitenlechner, M., Downard, A. J., Dunne, E. M., Flagan, R. C.,
938 Kajos, M., Keskinen, H., Kirkby, J., Kupc, A., Kürten, A., Kurtén, T., Laaksonen, A., Mathot, S.,
939 Onnela, A., Praplan, A. P., Rondo, L., Santos, F. D., Schallhart, S., Schnitzhofer, R., Sipilä, M.,
940 Tomé, A., Tsagkogeorgas, G., Vehkamäki, H., Wimmer, D., Baltensperger, U., Carslaw, K. S.,
941 Curtius, J., Hansel, A., Petäjä, T., Kulmala, M., Donahue, N. M., and Worsnop, D. R.: Molecular
942 understanding of atmospheric particle formation from sulfuric acid and large oxidized organic
943 molecules, *Proc. Natl. Acad. Sci.*, 110, 17223–17228, <https://doi.org/10.1073/pnas.1306973110>,
944 2013.
- 945 Sherwen, T., Schmidt, J. A., Evans, M. J., Carpenter, L. J., Großmann, K., Eastham, S. D., Jacob,
946 D. J., Dix, B., Koenig, T. K., Sinreich, R., Ortega, I., Volkamer, R., Saiz-Lopez, A., Prados-
947 Roman, C., Mahajan, A. S., and Ordóñez, C.: Global impacts of tropospheric halogens (Cl, Br, I)
948 on oxidants and composition in GEOS-Chem, *Atmospheric Chem. Phys.*, 16, 12239–12271,
949 <https://doi.org/10.5194/acp-16-12239-2016>, 2016a.
- 950 Sherwen, T. M., Evans, M. J., Spracklen, D. V., Carpenter, L. J., Chance, R., Baker, A. R.,
951 Schmidt, J. A., and Breider, T. J.: Global modeling of tropospheric iodine aerosol, *Geophys. Res.*
952 *Let.*, 43, 10012–10019, <https://doi.org/10.1002/2016GL070062>, 2016b.
- 953 Sipilä, M., Berndt, T., Petäjä, T., Brus, D., Vanhanen, J., Stratmann, F., Patokoski, J., Mauldin,
954 R. L., Hyvärinen, A.-P., Lihavainen, H., and Kulmala, M.: The Role of Sulfuric Acid in
955 Atmospheric Nucleation, *Science*, 327, 1243–1246, <https://doi.org/10.1126/science.1180315>,
956 2010.
- 957 Spracklen, D. V., Pringle, K. J., Carslaw, K. S., Chipperfield, M. P., and Mann, G. W.: A global
958 off-line model of size-resolved aerosol microphysics: I. Model development and prediction of
959 aerosol properties, *Atmospheric Chem. Phys.*, 5, 2227–2252, [https://doi.org/10.5194/acp-5-2227-](https://doi.org/10.5194/acp-5-2227-2005)
960 2005, 2005.
- 961 Thomas, M. A., Suntharalingam, P., Pozzoli, L., Rast, S., Devasthale, A., Kloster, S., Feichter, J.,
962 and Lenton, T. M.: Quantification of DMS aerosol-cloud-climate interactions using the
963 ECHAM5-HAMMOZ model in a current climate scenario, *Atmospheric Chem. Phys.*, 10, 7425–
964 7438, <https://doi.org/10.5194/acp-10-7425-2010>, 2010.
- 965 Trivitayanurak, W., Adams, P. J., Spracklen, D. V., and Carslaw, K. S.: Tropospheric aerosol
966 microphysics simulation with assimilated meteorology: model description and intermodel

967 comparison, *Atmospheric Chem. Phys.*, 8, 3149–3168, <https://doi.org/10.5194/acp-8-3149-2008>,
968 2008.

969 Urbanski, S. P. and Wine, P. H.: Spectroscopic and Kinetic Study of the Cl–S(CH₃)₂ Adduct, *J.*
970 *Phys. Chem. A*, 103, 10935–10944, <https://doi.org/10.1021/jp992682m>, 1999.

971 Vehkamäki, H., Kulmala, M., Napari, I., Lehtinen, K. E. J., Timmreck, C., Noppel, M., and
972 Laaksonen, A.: An improved parameterization for sulfuric acid–water nucleation rates for
973 tropospheric and stratospheric conditions, *J. Geophys. Res. Atmospheres*, 107, AAC 3-1-AAC 3-
974 10, <https://doi.org/10.1029/2002JD002184>, 2002.

975 Veres, P. R., Neuman, J. A., Bertram, T. H., Assaf, E., Wolfe, G. M., Williamson, C. J.,
976 Weinzierl, B., Tilmes, S., Thompson, C. R., Thames, A. B., Schroder, J. C., Saiz-Lopez, A.,
977 Rollins, A. W., Roberts, J. M., Price, D., Peischl, J., Nault, B. A., Møller, K. H., Miller, D. O.,
978 Meinardi, S., Li, Q., Lamarque, J.-F., Kupc, A., Kjaergaard, H. G., Kinnison, D., Jimenez, J. L.,
979 Jernigan, C. M., Hornbrook, R. S., Hills, A., Dollner, M., Day, D. A., Cuevas, C. A.,
980 Campuzano-Jost, P., Burkholder, J., Bui, T. P., Brune, W. H., Brown, S. S., Brock, C. A.,
981 Bourgeois, I., Blake, D. R., Apel, E. C., and Ryerson, T. B.: Global airborne sampling reveals a
982 previously unobserved dimethyl sulfide oxidation mechanism in the marine atmosphere, *Proc.*
983 *Natl. Acad. Sci.*, 117, 4505–4510, <https://doi.org/10.1073/pnas.1919344117>, 2020.

984 Vermeuel, M. P., Novak, G. A., Jernigan, C. M., and Bertram, T. H.: Diel Profile of
985 Hydroperoxymethyl Thioformate: Evidence for Surface Deposition and Multiphase Chemistry,
986 *Environ. Sci. Technol.*, 54, 12521–12529, <https://doi.org/10.1021/acs.est.0c04323>, 2020.

987 Wang, W.-L., Song, G., Primeau, F., Saltzman, E. S., Bell, T. G., and Moore, J. K.: Global ocean
988 dimethyl sulfide climatology estimated from observations and an artificial neural network,
989 *Biogeosciences*, 17, 5335–5354, <https://doi.org/10.5194/bg-17-5335-2020>, 2020.

990 Wang, X., Jacob, D. J., Eastham, S. D., Sulprizio, M. P., Zhu, L., Chen, Q., Alexander, B.,
991 Sherwen, T., Evans, M. J., Lee, B. H., Haskins, J. D., Lopez-Hilfiker, F. D., Thornton, J. A.,
992 Huey, G. L., and Liao, H.: The role of chlorine in global tropospheric chemistry, *Atmospheric*
993 *Chem. Phys.*, 19, 3981–4003, <https://doi.org/10.5194/acp-19-3981-2019>, 2019.

994 Wang, X., Jacob, D. J., Downs, W., Zhai, S., Zhu, L., Shah, V., Holmes, C. D., Sherwen, T.,
995 Alexander, B., Evans, M. J., Eastham, S. D., Neuman, J. A., Veres, P. R., Koenig, T. K.,
996 Volkamer, R., Huey, L. G., Bannan, T. J., Percival, C. J., Lee, B. H., and Thornton, J. A.: Global
997 tropospheric halogen (Cl, Br, I) chemistry and its impact on oxidants, *Atmospheric Chem. Phys.*,
998 21, 13973–13996, <https://doi.org/10.5194/acp-21-13973-2021>, 2021.

999 Wang, Y., Jacob, D. J., and Logan, J. A.: Global simulation of tropospheric O₃-NO_x -
1000 hydrocarbon chemistry: 1. Model formulation, *J. Geophys. Res. Atmospheres*, 103, 10713–
1001 10725, <https://doi.org/10.1029/98JD00158>, 1998.

1002 Wesely, M. L.: Parameterization of surface resistances to gaseous dry deposition in regional-
1003 scale numerical models, *Atmospheric Environ.* 1967, 23, 1293–1304,
1004 [https://doi.org/10.1016/0004-6981\(89\)90153-4](https://doi.org/10.1016/0004-6981(89)90153-4), 1989.

- 1005 Westervelt, D. M., Pierce, J. R., Riipinen, I., Trivitayanurak, W., Hamed, A., Kulmala, M.,
1006 Laaksonen, A., Decesari, S., and Adams, P. J.: Formation and growth of nucleated particles into
1007 cloud condensation nuclei: model–measurement comparison, *Atmospheric Chem. Phys.*, 13,
1008 7645–7663, <https://doi.org/10.5194/acp-13-7645-2013>, 2013.
- 1009 Williamson, C. J., Kupc, A., Axisa, D., Bilsback, K. R., Bui, T., Campuzano-Jost, P., Dollner,
1010 M., Froyd, K. D., Hodshire, A. L., Jimenez, J. L., Kodros, J. K., Luo, G., Murphy, D. M., Nault,
1011 B. A., Ray, E. A., Weinzierl, B., Wilson, J. C., Yu, F., Yu, P., Pierce, J. R., and Brock, C. A.: A
1012 large source of cloud condensation nuclei from new particle formation in the tropics, *Nature*,
1013 574, 399–403, <https://doi.org/10.1038/s41586-019-1638-9>, 2019.
- 1014 Wollesen de Jonge, R., Elm, J., Rosati, B., Christiansen, S., Hyttinen, N., Lüdemann, D., Bilde,
1015 M., and Roldin, P.: Secondary aerosol formation from dimethyl sulfide – improved mechanistic
1016 understanding based on smog chamber experiments and modelling, *Atmospheric Chem. Phys.*,
1017 21, 9955–9976, <https://doi.org/10.5194/acp-21-9955-2021>, 2021.
- 1018 Wu, R., Wang, S., and Wang, L.: New Mechanism for the Atmospheric Oxidation of Dimethyl
1019 Sulfide. The Importance of Intramolecular Hydrogen Shift in a CH₃SCH₂OO Radical, *J. Phys.*
1020 *Chem. A*, 119, 112–117, <https://doi.org/10.1021/jp511616j>, 2015.
- 1021 Zhang, J.-Z. and Millero, F. J.: The products from the oxidation of H₂S in seawater, *Geochim.*
1022 *Cosmochim. Acta*, 57, 1705–1718, [https://doi.org/10.1016/0016-7037\(93\)90108-9](https://doi.org/10.1016/0016-7037(93)90108-9), 1993.
- 1023 Zhang, Y., Jacob, D. J., Maasackers, J. D., Sulprizio, M. P., Sheng, J.-X., Gautam, R., and
1024 Worden, J.: Monitoring global tropospheric OH concentrations using satellite observations of
1025 atmospheric methane, *Atmospheric Chem. Phys.*, 18, 15959–15973, [https://doi.org/10.5194/acp-](https://doi.org/10.5194/acp-18-15959-2018)
1026 18-15959-2018, 2018.
- 1027 Zhou, Z.-X., Lujan, S. A., Burkholder, A. B., Garbacz, M. A., and Kunkel, T. A.: Roles for DNA
1028 polymerase δ in initiating and terminating leading strand DNA replication, *Nat. Commun.*, 10,
1029 3992, <https://doi.org/10.1038/s41467-019-11995-z>, 2019.
- 1030 Zhu, L., Nicovich, J. M., and Wine, P. H.: Temperature-dependent kinetics studies of aqueous
1031 phase reactions of hydroxyl radicals with dimethylsulfoxide, dimethylsulfone, and
1032 methanesulfonate, *Aquat. Sci.*, 65, 425–435, <https://doi.org/10.1007/s00027-003-0673-6>, 2003.
- 1033 Zhu, L., Nenes, A., Wine, P. H., and Nicovich, J. M.: Effects of aqueous organosulfur chemistry
1034 on particulate methanesulfonate to non–sea salt sulfate ratios in the marine atmosphere, *J.*
1035 *Geophys. Res. Atmospheres*, 111, <https://doi.org/10.1029/2005JD006326>, 2006.
- 1036 Zhu, L., Jacob, D. J., Eastham, S. D., Sulprizio, M. P., Wang, X., Sherwen, T., Evans, M. J.,
1037 Chen, Q., Alexander, B., Koenig, T. K., Volkamer, R., Huey, L. G., Le Breton, M., Bannan, T.
1038 J., and Percival, C. J.: Effect of sea salt aerosol on tropospheric bromine chemistry, *Atmospheric*
1039 *Chem. Phys.*, 19, 6497–6507, <https://doi.org/10.5194/acp-19-6497-2019>, 2019.
- 1040